Longitudinal dispersion of turbulent oscillatory pipe flows

Song, Jie; Law, Adrian Wing-Keung

2014

Longitudinal Dispersion of Turbulent Oscillatory Pipe Flows

Jie Song[1,2], Adrian Wing-Keung Law[1,2,3*]

[1]School of Civil and Environmental Engineering, Nanyang Technological University, 50 Nanyang Avenue, Singapore 639798

[2]Singapore Membrane Technology Centre, Nanyang Environment and Water Research Institute, Nanyang Technological University, 1 Cleantech Loop, Singapore 637141

[3]DHI-NTU Centre, Nanyang Environment and Water Research Institute, Nanyang Technological University, 1 Cleantech Loop, Singapore 637141

* Email address for correspondence: cwklaw@ntu.edu.sg

Abstract

In the present study, we examine the longitudinal dispersion of oscillatory pipe flows in the turbulent range which is not well covered before. An analytical analysis was first performed using the homogenization approach (i.e. multiple scale perturbation analysis) to predict the magnitude of the longitudinal dispersion induced by a turbulent oscillatory flow forced by a sinusoidal pressure gradient inside a circular pipe. An axisymmetric co-axial eddy viscosity model was adopted to resolve the radial distribution of velocities and turbulent shear stresses. Based on the derived kinematic characteristics, the longitudinal dispersion coefficient for the turbulent oscillatory pipe flow was then quantified. The results demonstrated that a dimensionless parameter α, which is the ratio of the oscillatory velocity amplitude divided by the frequency and pipe radius, determines the flow structure as well as the magnitude of the induced longitudinal dispersion coefficient. Experiments were also conducted to quantify the longitudinal dispersion coefficient under different frequencies and oscillatory velocity magnitudes. The measurement approaches were based on the non-invasive laser imaging techniques of Particle Image Velocimetry and Planar Laser Induced Fluorescence. The experimental conditions covered a relatively wide range of boundary Reynolds number (Re_δ) from 100 to 1000, and included both laminar and turbulent flow regimes. The results showed that when the flow enters the so-called conditional turbulence regime, i.e. $\mathrm{Re}_\delta \geq 500$, the longitudinal dispersion coefficient increases drastically. The analytical predictions based on the homogenization approach in the present study agree well with the measured longitudinal dispersion coefficients.

1. Introduction

The classical analysis of longitudinal dispersion in a steady laminar pipe flow can be traced back to Taylor [1], who showed that the dispersion is significantly enhanced in the longitudinal direction due to the non-uniform cross-sectional velocity profile inside the pipe. Hence, the longitudinal dispersion is also sometimes referred as Taylor dispersion. Dispersion in steady turbulent pipe flows was also later examined by Taylor [2], who showed that the dispersion coefficient is related to the pipe geometry as well as the friction velocity. Since then, many studies had further investigated the longitudinal dispersion of steady flows in different settings. A good summary can be found in Fischer et al. [3].

Besides steady flows, the longitudinal dispersion in unsteady laminar oscillatory flows, whereby the passive solute particles undergo simultaneous diffusion and convection driven by a periodic pressure gradient, was also extensively investigated (e.g. [4-6]). Generally, the dispersion coefficient was found to be dependent on the oscillating frequency, velocity magnitude, cross-sectional geometry and Schmidt number. An analytical solution of the longitudinal dispersion coefficient due to the combined effect of steady and periodic flows within a conduit of uniform cross-section was also obtained by Mukherjee and Mazumder [7]. Joshi et al. [8] performed experiments on gas exchange in laminar oscillatory flows within a circular pipe. Their results showed good agreement with the theoretical predictions by Watson [6]. Pedley and Kamm [9] found that for the axial mass transport in an oscillatory pipe flow with steady secondary flow, a maximum transport rate can be achieved when the secondary-flow time equals the oscillation period. In recent years, the dispersion analysis has also been extended to more complicated situations, for example, in pipes with reactive walls [10-13], in curved pipes [14-16], in pipes with chemically reactive solute [17], and with

grooved cross-sectional geometry [18]. Most recently, Mei et al. [19] analytically investigated the longitudinal dispersion of laminar oscillatory flows driven by multiple frequencies. By examining the related configuration of a pressure exchanger for seawater desalination, and assuming that the flow inside the ducts is laminar, Mei et al. [19] showed that the long term mixing inside the exchangers is very small between the feed water and the brine.

Comparing with laminar oscillatory flows, the longitudinal dispersion in turbulent oscillatory pipe flows is rarely reported in the literature both analytically or experimentally. Mondal and Mazumder [20] examined the stream-wise dispersion of fine suspended particles in a turbulent oscillatory flow from an elevated source. It was shown that the iso-concentration lines can be affected by the settling velocity, oscillation frequency and velocity magnitude, and source height. Lee [21] performed experiments to qualitatively visualize the mixing of smoke inside the turbulent oscillatory pipe flow. The results suggested that the turbulence affects the radial mixing considerably as the Reynolds number increases. Ye and Zhang [22] examined the effect of turbulence on the Taylor dispersion for oscillatory pipe flows using laser techniques. They found that the longitudinal dispersion can be significantly enhanced by the turbulence by orders of magnitude. Their results will be discussed further in the later part of this paper. Zhou et al. [23] proposed a 2D axisymmetric CFD model with k-ε turbulence closure to simulate the mixing inside an isobaric pressure exchanger due to oscillatory flows inside the exchanger ducts. Their results showed that steady mixing can be established in the duct flows within a short time. Recently, Liu et al. [24] extended to a three-dimensional numerical model with RNG k-ε turbulence closure to analyze the effect of flow velocity and angular frequency on the mixing inside the pressure exchanger. Quantitative results on the mixing coefficient were obtained. Although both numerical studies were performed carefully,

the analysis was specific to the geometry involved, and it was also unclear whether the k-ε closure itself affected the quantitative determination of the mixing involved.

Unlike axisymmetric pipe flows, the longitudinal dispersion effect is studied more extensively under surface gravity waves for both laminar and turbulent boundary layers at the bottom with a typical two-dimensional planar setting. Mei and Chian [25] and Ng and Wu [26] investigated the dispersion of suspended particles in wavy boundary layers. Trowbridge and Madsen [27] proposed a time-varying eddy viscosity model to study the turbulent wave-induced near-bottom boundary layers, and applied the model to analyze the wave-induced mass transport [28]. Although their model is relatively simple compared to the turbulence closures in CFD models nowadays, it is able to yield analytical results that match the reported laboratory data in a satisfactory manner. This model has also been adopted by both Ng [29] and Mazumder and Paul [30] to investigate the longitudinal dispersion in a two-dimensional turbulent oscillatory channel flow and dispersion of settling particles in oscillatory turbulent flow with effect of deposition and re-entrainment, respectively.

In the present study, the longitudinal dispersion of turbulent oscillatory pipe flows was investigated both analytically and experimentally. We first adopted an axisymmetric co-axial eddy viscosity model that is similar to the two-layer model of Trowbridge and Madsen [27], to examine the turbulent oscillatory flows inside the circular pipe. A perturbation analysis was then performed based on the homogenization technique with multiple scales. The approach and analysis thus bear similarity to Ng [29], however the cylindrical setting generates analytical solutions of very different forms. In addition, experiments using the advanced non-invasive image techniques of Particle Image Velocimetry (PIV) and Planar Laser Induced Fluorescence (PLIF) were conducted to quantify the longitudinal dispersion coefficient under different combinations of frequency and oscillatory velocity magnitude.

The experimental parameters covered a wide range of boundary Reynolds number from 100 to 1000, and included both laminar and turbulent flow regimes. The experimental results were then compared with the theoretical predictions by the homogenization technique. In the following, we shall first present the analytical analysis before discussing the experimental results and comparison.

2. Theory

2.1 Turbulent oscillatory flow in a circular pipe

We adopt a cylindrical coordinate for the pipe flow, as shown in Figure 1. The x-axis is the axial direction, and r is the radical direction with $r = 0$ at the centreline. The axial velocity u varies with time t and radius r, i.e. $u = u(r,t)$, while the pressure p is changing with t and x (i.e. only the axial pressure gradient is considered, which should be valid for small diameters). In this manner, the Navier-Stokes equation in the cylindrical form can be reduced to:

$$\frac{\partial u}{\partial t} = -\frac{1}{\rho}\frac{\partial p}{\partial x} - \frac{1}{\rho}\frac{1}{r}\frac{\partial(r\tau)}{\partial r} \tag{1}$$

where ρ is the fluid density and τ the turbulent Reynolds stress, which can be related to the velocity gradient by the eddy viscosity ν_T in the form [27],

$$\tau = -\rho\nu_T\frac{\partial u}{\partial r} \tag{2}$$

At the wall boundary, the velocity is assumed to be zero at $r = a - r_0$ due to the no-slip condition, i.e.

$$u = 0 \text{ at } r = a - r_0 \tag{3a}$$

where a is the pipe radius. For a rough wall, r_0 represents the wall roughness and is typically taken to be $r_0 = k_b / 30$, where k_b is the equivalent Nikuradse roughness. For a smooth wall, however, r_0 is not the true roughness but rather denotes the embedded viscous sub-layer thickness, and usually is in the order of 10^{-5} m.

Due to axisymmetry, the velocity gradient vanishes at the centreline, i.e.

$$\frac{\partial u}{\partial r} = 0 \text{ at } r = 0 \tag{3b}$$

We consider a purely oscillatory flow with a single frequency and without any steady component. In this case, the pressure gradient is then independent of both x and r, and only changes with time t, which can be expressed as:

$$-\frac{1}{\rho}\frac{\partial p}{\partial x} = P\cos(\omega t) = P \cdot \mathrm{Re}\left[e^{i\omega t}\right] \tag{4}$$

where ω is the oscillation angular frequency, P is the amplitude of the pressure gradient, $\mathrm{Re}[\ ]$ denotes the real part of the complex expression, and $i = \sqrt{-1}$. Equation (4) implies that both the velocity u and the shear stress τ are purely sinusoidal with a period of T ($T = \frac{2\pi}{\omega}$). Hence these quantities can be expressed by the following Fourier expansions with only odd harmonics of the fundamental frequency,

$$u = \mathrm{Re}\left[u^{(1)}e^{i\omega t} + u^{(3)}e^{3i\omega t} + ...\right] \tag{5}$$

$$\tau = \mathrm{Re}\left[\tau^{(1)}e^{i\omega t} + \tau^{(3)}e^{3i\omega t} + ...\right] \tag{6}$$

where $u^{(1)}, \tau^{(1)},...$ are complex functions of r.

The above forms of equations also imply that ν_T contains only even harmonics of the fundamental frequency according to (2), i.e.

$$\nu_T = \nu^{(0)} \cdot \mathrm{Re}\left[1 + a^{(2)}e^{2i\omega t} + ...\right] \tag{7}$$

where $\nu^{(0)}$ is a real function of r representing the time-averaged value of the eddy viscosity, and $a^{(2)}$ is a complex constant representing the time variation of ν_T.

Earlier, Trowbridge and Madsen [27] had shown that the time-varying part of the eddy viscosity is small in comparison with the time-averaged part, and the third-harmonic components of velocity and shear stress are smaller than the first-harmonic components, i.e.

$$\left|a^{(2)}\right|, \frac{u^{(3)}}{u^{(1)}}, \frac{\tau^{(3)}}{\tau^{(1)}} = \mathrm{O}(\varepsilon) \tag{8}$$

where ε is a small parameter.

Substituting (2), (4), (5) and (7) into (1), the governing equations for the Fourier components can then be derived as:

$$u^{(1)}i\omega = P + \frac{1}{r}\frac{d}{dr}\left(r\nu^{(0)}\frac{du^{(1)}}{dr}\right) + \frac{a^{(2)}}{2}\frac{1}{r}\frac{d}{dr}\left(r\nu^{(0)}\frac{du_*^{(1)}}{dr}\right) \tag{9}$$

$$3u^{(3)}i\omega = \frac{1}{r}\frac{d}{dr}\left(r\nu^{(0)}\frac{du^{(3)}}{dr}\right) + \frac{a^{(2)}}{2}\frac{1}{r}\frac{d}{dr}\left(r\nu^{(0)}\frac{du^{(1)}}{dr}\right) \tag{10}$$

where the asterisk denotes the complex conjugate. The boundary conditions are modified accordingly as follow:

$$u^{(1)} = u^{(3)} = 0 \text{ at } r = a - r_0 \tag{11a}$$

8

$$\frac{du^{(1)}}{dr} = \frac{du^{(3)}}{dr} = 0 \text{ at } r = 0 \tag{11b}$$

We now adopt an axisymmetrical co-axial model to represent the time-averaged part of the eddy viscosity. The approach is similar to the two-layer planar model introduced by Trowbridge and Madsen [27]. In this model, $v^{(0)}$ (which is related to the time-averaged wall shear stress) is the product of a local length scale and velocity scale in the near wall region, while becomes a constant in the outer region, i.e.

$$v^{(0)} = \kappa \overline{u_f} \begin{cases} (a - r) & a - \delta_I < r < a \\ \\ \delta_I & 0 \le r \le a - \delta_I \end{cases} \tag{12}$$

where $\kappa = 0.4$ is the von Karman's constant, $\overline{u_f}$ the friction velocity, and δ_I the thickness of the inner boundary layer (which is typically taken as one sixth of the characteristic boundary layer thickness δ, defined by $\frac{\kappa \overline{u_f}}{\omega}$). Since the maximum boundary layer thickness inside the circular pipe would be the pipe radius itself, thus the thickness can be expressed as,

$$\delta_I = \frac{1}{6} \min(a, \frac{\kappa \overline{u_f}}{\omega}) \tag{13}$$

In order to simplify the analysis, it is more convenient to switch the coordinate from r to s, where $s = a - r$. Substituting (12) into (9) and (10) and normalizing all the variables, the governing equations (9) and (10) in the non-dimensional form become (using a prime to denote non-dimensional variables):

$$\frac{\alpha \overline{u_f}'}{1 - s'} \frac{d}{ds'} \left((1 - s')\beta \frac{du^{(1)'}}{ds'} \right) - iu^{(1)'} = -1 - \frac{a^{(2)}}{2} \frac{\alpha \overline{u_f}'}{1 - s'} \frac{d}{ds'} \left((1 - s')\beta \frac{du_*^{(1)'}}{ds'} \right) \tag{14}$$

$$\frac{\alpha \overline{u_f}'}{1-s'}\frac{d}{ds'}\left((1-s')\beta\frac{du^{(3)'}}{ds'}\right)-3iu^{(3)'}=-\frac{a^{(2)}}{2}\frac{\alpha \overline{u_f}'}{1-s'}\frac{d}{ds'}\left((1-s')\beta\frac{du^{(1)'}}{ds'}\right)$$ (15)

with the following boundary conditions:

$$u^{(1)'}=u^{(3)'}=0 \text{ at } s'=r_0'$$ (16a)

$$\frac{du^{(1)'}}{ds'}=\frac{du^{(3)'}}{ds'}=0 \text{ at } s'=1$$ (16b)

where, $(u^{(1)'},u^{(3)'},\overline{u_f}')=(u^{(1)},u^{(3)},\overline{u_f})/U$ (U is a characteristic velocity defined by $\frac{P}{\omega}$), $(s',r_0')=(s,r_0)/a$ and $t'=t\omega$ are non-dimensional variables. α is a non-dimensional control parameter in the form of $\alpha=\frac{kU}{\omega a}$, and $\beta=\min(s',\delta_I')$, where the non-dimensional inner boundary layer thickness $\delta_I'=\frac{1}{6}\min(1,\alpha\overline{u_f}')$ is as discussed above.

To solve for the governing equations (14) and (15), we need to introduce the auxiliary solutions $F^{(n)}$, $(n=1,3)$, which satisfy the corresponding homogeneous differential equation,

$$\frac{\alpha \overline{u_f}'}{1-s'}\frac{d}{ds'}\left((1-s')\beta\frac{dF^{(n)}}{ds'}\right)-inF^{(n)}=0$$ (17)

Since β is not analytical at $s'=\delta_I'$, (17) needs to be solved separately within the inner boundary layer and in the outer region, with the matching requirements for the velocity and shear stress solutions at $s'=\delta_I'$, i.e.

$$F^{(n)}(\delta_I'^-)=F^{(n)}(\delta_I'^+)$$ (18a)

$$\frac{dF^{(n)}(\delta_I'^-)}{ds'}=\frac{dF^{(n)}(\delta_I'^+)}{ds'}$$ (18b)

10

Together with the outer-edge boundary condition:

$$\frac{dF^{(n)}(1)}{ds'} = 0 \tag{19}$$

The complex auxiliary functions $F^{(n)}$ can then be derived analytically as shown in Appendix A.

With the wall boundary condition $u^{(1)'}(r_0') = 0$, the solutions of (14) and (15) can be expressed by the auxiliary functions $F^{(n)}$ as:

$$u^{(1)'} = i\left(\frac{F^{(1)}}{F^{(1)}(r_0')} - 1\right) + \frac{ia^{(2)}}{4}\left(\frac{F_*^{(1)}}{F_*^{(1)}(r_0')} - \frac{F^{(1)}}{F^{(1)}(r_0')}\right) + O(\varepsilon^2) \tag{20}$$

$$u^{(3)'} = \frac{ia^{(2)}}{4}\left(\frac{F^{(1)}}{F^{(1)}(r_0')} - \frac{F^{(3)}}{F^{(3)}(r_0')}\right) + O(\varepsilon^2) \tag{21}$$

Expressions for the Fourier components of the shear stress can then be obtained accordingly as:

$$\tau^{(1)'} = i\kappa\overline{u_f}'\beta\left[\frac{dF^{(1)}/ds'}{F^{(1)}(r_0')} - \frac{a^{(2)}}{4}\left(\frac{dF_*^{(1)}/ds'}{F_*^{(1)}(r_0')} + \frac{dF^{(1)}/ds'}{F^{(1)}(r_0')}\right) + O(\varepsilon^2)\right] \tag{22}$$

$$\tau^{(3)'} = \frac{1}{4}i\kappa\overline{u_f}'\beta a^{(2)}\left[3\frac{dF^{(1)}/ds'}{F^{(1)}(r_0')} - \frac{dF^{(3)}/ds'}{F^{(3)}(r_0')}\right] + O(\varepsilon^2) \tag{23}$$

To derive the velocities and shear stresses, the unknown friction velocity $\overline{u_f}'$ and the constant $a^{(2)}$ need to be resolved. Earlier, Trowbridge and Madsen [27] had shown that $\overline{u_f}'$ and $\overline{u_f}'a^{(2)}$ can be linked to the instantaneous wall shear stress in the following manner,

$$\overline{u_f}' = \left|\tau_b^{(1)'}\right|^{1/2}\frac{1}{\sqrt{\pi}}\frac{\Gamma\left(\frac{3}{4}\right)}{\Gamma\left(\frac{5}{4}\right)}\left[1 - \frac{3}{10}\mathrm{Re}\left(\frac{\tau_b^{(3)'}\tau_{b*}^{(1)'}}{\tau_b^{(1)'}\tau_b^{(1)'}}\right) + O(\varepsilon^2)\right] \tag{24}$$

$$\overline{u_f}'a^{(2)} = \frac{1}{\sqrt{\pi}} \frac{2}{5} \left| \tau_b^{(1)'} \right|^{1/2} \frac{\Gamma\left(\frac{3}{4}\right)}{\Gamma\left(\frac{5}{4}\right)} \frac{\tau_b^{(1)'}}{\tau_{b*}^{(1)'}} + O(\varepsilon) \tag{25}$$

where Γ is the Gamma function. Combining (24) and (25), we obtain the leading term as:

$$a^{(2)} = \frac{2}{5} \frac{\tau_b^{(1)'}}{\tau_{b*}^{(1)'}} \tag{26}$$

By applying the limit at the wall, $\displaystyle\lim_{s'\to 0} s' \frac{dF^{(n)}}{ds'}$, to (22) and (23), we can obtain $\tau_b^{(1)'}$ and $\tau_b^{(3)'}$ as a function of $\overline{u_f}'$ for specific α. Substituting $\tau_b^{(1)'}$ and $\tau_b^{(3)'}$ into (24) and (26), $a^{(2)}$ can be computed and $\overline{u_f}'$ can be solved iteratively. The Fourier components of the velocity and shear stress can then be obtained by substituting the value of $\overline{u_f}'$ and $a^{(2)}$ into (20) to (23). And both the velocity profiles and distribution of shear stresses in non-dimensional form can be fully resolved. The procedural steps described are similar to the planar case shown in Ng [29].

The non-dimensional parameter r_0' related to r_0 and a, and thus can vary over a large range for various pipe radius. As mentioned previously, r_0 is usually in the order of 10^{-5} m. Meanwhile, a pipe with a relatively larger diameter of $O(10^{-2})$ m was used in the following experiments for visualisation. Here, we present the numerical computations based on $r_0' = 0.001$ and 0.005 so that they can be compared with the experimental results later on. The results for the friction velocity $\overline{u_f}'$, the complex constant $a^{(2)}$ and the inner boundary layer thickness δ_I' are plotted in Figure 2 as functions of α, where the solid and dashed curves represent $r_0' = 0.001$ and 0.005, respectively. Figure 2(a) clearly illustrates that $\overline{u_f}'$

decreases monotonically with α. Also, with small α, $\overline{u_f}'$ with the larger roughness of $r_0' = 0.005$ is higher than that of $r_0' = 0.001$, however, the difference becomes negligible when α exceeds 100. In Figure 2(b), both the real and imaginary parts of $a^{(2)}$ oscillate with α with an amplitude less than 0.4, which generally validates the assumption made in (8), although the higher order terms will be relatively more significant with a larger $a^{(2)}$. Figure 2(c) shows that the inner boundary layer thickness increases with α first (δ_I' with $r_0' = 0.001$ is smaller than with $r_0' = 0.005$) and becomes a constant of 1/6 when α reaches ~20. The change-over point for $r_0' = 0.005$ occurs at smaller α than that for $r_0' = 0.001$, which suggests that the boundary layer thickness extends to the centreline of the pipe earlier at larger r_0'.

Based on the information from Figure 2, the profiles of eddy viscosity, velocity and shear stress at various phases within an oscillation period are shown in Figures 3, 4 and 5, respectively. In each figure, a comparison is made among α =0.5, 5, 50 and 500 to illustrate the effect of α. The results for $r_0' = 0.001$ and 0.005 are also listed in the figures from (a)-(d) and (e)-(h) respectively for comparison. Since α is inversely proportional to ω, by keeping U and a constant, we expect a smaller α when the flow oscillates faster. In Figure 3, for the first two cases, i.e. α =0.5 and 5, when the oscillation frequency is relatively high, it can be observed that the boundary layer is thin; while for the last two cases, the boundary layer thickness extends fully to the centreline and δ_I' reaches the maximum value of 1/6. It is obvious from Figure 4 that with small α (i.e. Figures 4(a) and 4(e)), a strong phase lag exists between the flow within the boundary layer (where the velocity decreases towards the wall) and in the outer region (where the flow behaves as a plug flow). This is reasonable as under high frequency oscillations, the velocity inside the boundary layer does not react to the

pressure gradient immediately due to inertia. As α increases, the flow becomes more uniform over the cross-section. It can also be inferred that for all the cases, the velocity gradient under $r_0' = 0.005$ is smaller comparing to $r_0' = 0.001$. The same trend can be noted in Figure 5. The shear stress distribution becomes more linear as α increases.

2.2 Longitudinal Dispersion Coefficient

After the flow characteristics are determined above, we proceed to analyze the longitudinal dispersion in the turbulent oscillatory pipe flow in this section. We start by considering a finite cloud of mass dissolved homogeneously over the cross-section inside the turbulent oscillatory pipe flow. Driven by advection, the centre of the cloud will then move forward and backward periodically with a zero net displacement. During this process, however, the cloud expands due to the turbulent dispersion and more importantly, the dispersion induced by the turbulent shear flow. In the following, we shall analyze the longitudinal dispersion based on the homogenization method described in details by Mei and Vernescu [31].

Since the flow is only in the x direction, the scalar transport in a circular pipe is governed by the convection-diffusion equation in the cylindrical coordinates:

$$\frac{\partial C}{\partial t} + u\frac{\partial C}{\partial x} = D_t \frac{\partial^2 C}{\partial x^2} + \frac{1}{r}\frac{\partial}{\partial r}\left(rD_t \frac{\partial C}{\partial r} \right) \tag{27}$$

subject to the boundary condition:

$$\frac{\partial C}{\partial r} = 0 \text{ at } r = 0, a - r_0 \tag{28}$$

where C is the scalar concentration, and D_t is the turbulent dispersivity which is assumed to be isotropic in all directions.

14

The turbulent dispersivity is taken to be related to the eddy viscosity through the turbulent Schmidt number, which is the ratio of the two, i.e. $Sc = \nu_T / D_t$. In the literature, it was found that the turbulent Schmidt number is in the order of unity based on experimental measurements [32, 33]. Since we are interested in the long term behaviour of the longitudinal dispersion, hence we examine the case with the turbulent dispersivity being proportional to the time-averaged eddy viscosity, $\nu^{(0)}$, i.e.

$$D_t = \phi \nu^{(0)} \tag{29}$$

where $\phi = O(1)$.

We consider the situation that the pipe radius is sufficiently small such that the concentration becomes homogeneous over the cross-section after a few oscillations in the turbulent regime, i.e.

$$\frac{2\pi}{\omega} \sim \frac{a^2}{D_t} \tag{30}$$

Furthermore, we assume that the longitudinal length scale L is much larger than the pipe radius, which is,

$$\eta = a / L << 1 \tag{31}$$

where η denotes a parameter much smaller than one. Note that this is the condition whereby the homogenization technique can be strictly applied, although in reality the results are similar even for larger η in many cases. Based on the assumptions of (30) and (31), the governing equation (27) can be rewritten using η to indicate the order of magnitude of each term,

$$\frac{\partial C}{\partial t} + \eta u \frac{\partial C}{\partial x} = \eta^2 D_t \frac{\partial^2 C}{\partial x^2} + \frac{1}{r}\frac{\partial}{\partial r}\left(rD_t \frac{\partial C}{\partial r}\right) \tag{32}$$

We now introduce the homogenization approach with the multiple-scale perturbation analysis. Typically, three sharply distinct time scales t, t_1 and t_2 need to be adopted to represent the three different transport processes, i.e. dispersion over the cross-section, advection and dispersion along the longitudinal direction, respectively. However, for purely oscillatory flows (i.e. net advection does not exist), the intermediate time scale is not of significance, hence, we only apply the two time scales, t and t_2, in the present study (note however that the result is the same as that by applying the three time scales), i.e.

$$t, t_2 = \eta^2 t \tag{33}$$

In the same manner, the concentration and time derivative can be expanded as:

$$C = C_0 + \eta C_1 + \eta^2 C_2 + \dots \tag{34}$$

$$\frac{\partial}{\partial t} = \frac{\partial}{\partial t} + \eta^2 \frac{\partial}{\partial t_2} + \dots \tag{35}$$

At $O(1)$, the leading order concentration C_0 has been proven to be independent of r and t [31], i.e.

$$C_0 = C_0(x, t_2) \tag{36}$$

At $O(\eta)$, the concentration C_1 is governed by:

$$\frac{\partial C_1}{\partial t} + u \frac{\partial C_0}{\partial x} = \frac{1}{r}\frac{\partial}{\partial r}\left(rD_t \frac{\partial C_1}{\partial r}\right) \tag{37}$$

Substituting (5) for u and (29) for D_t, the above equation becomes:

16

$$\frac{\partial C_1}{\partial t} + \text{Re}\left[u^{(1)}e^{i\omega t}\right]\frac{\partial C_0}{\partial x} = \frac{\phi}{r}\frac{\partial}{\partial r}\left(rv^{(0)}\frac{\partial C_1}{\partial r}\right) \tag{38}$$

with the boundary condition:

$$\frac{\partial C_1}{\partial r} = 0 \text{ at } r = 0, a - r_0 \tag{39}$$

In view of linearity, the first order concentration C_1 can be expressed as:

$$C_1 = \frac{\partial C_0}{\partial x}\text{Re}\left[B^{(1)}e^{i\omega t}\right] \tag{40}$$

where $B^{(1)}$ is a complex function of r. Substituting (40) into (38), we obtain the governing equation for $B^{(1)}$ as:

$$i\omega B^{(1)} + u^{(1)} = \frac{\phi}{r}\frac{d}{dr}\left(rv^{(0)}\frac{dB^{(1)}}{dr}\right) \tag{41}$$

with the boundary condition:

$$\frac{dB^{(1)}}{dr} = 0 \text{ at } r = 0, a - r_0 \tag{42}$$

Solving the function $B^{(1)}$ is the key towards the determination of the magnitude of the longitudinal dispersion coefficient.

We now proceed to consider $O(\eta^2)$. The governing equation is:

$$\frac{\partial C_0}{\partial t_2} + \frac{\partial C_2}{\partial t} + u\frac{\partial C_1}{\partial x} = D_t\frac{\partial^2 C_0}{\partial x^2} + \frac{1}{r}\frac{\partial}{\partial r}\left(rD_t\frac{\partial C_2}{\partial r}\right) \tag{43}$$

Substituting (40) into (43) yield:

$$\frac{\partial C_0}{\partial t_2} + \frac{\partial C_2}{\partial t} + \text{Re}\left[u^{(1)}e^{i\omega t}\right]\text{Re}\left[B^{(1)}e^{i\omega t}\right]\frac{\partial^2 C_0}{\partial x^2} = D_t\frac{\partial^2 C_0}{\partial x^2} + \frac{1}{r}\frac{\partial}{\partial r}\left(rD_t\frac{\partial C_2}{\partial r}\right) \tag{44}$$

Taking the time and cross-sectional average of (44) and after some rearrangement, we obtain the effective scalar transport equation as:

$$\frac{\partial C_0}{\partial t_2} = \left\{ \langle D_t \rangle - \frac{1}{2} \text{Re} \langle u^{(1)} B_*^{(1)} \rangle \right\} \frac{\partial^2 C_0}{\partial x^2} \tag{45}$$

where the angular brackets $\langle \ \rangle$ represent the cross-sectional average.

The second term on the RHS of (45) gives rise to the longitudinal dispersion [29, 31]. We define the longitudinal dispersion coefficient in an oscillatory flow with zero time-averaged velocity as,

$$D_l = -\frac{1}{2} \text{Re} \langle u^{(1)} B_*^{(1)} \rangle \tag{46}$$

Recalling the governing equation (41) and normalizing all the variables and parameters with the change of the coordinate from r' to s' as before, we have

$$\frac{\phi \alpha \overline{u_f}'}{1-s'} \frac{d}{ds'} \left((1-s')\beta \frac{dB^{(1)'}}{ds'} \right) - iB^{(1)'} = u^{(1)'} \tag{47}$$

subject to the boundary condition:

$$\frac{dB^{(1)'}}{ds'} = 0 \ \text{ at } \ s'=1, r_0' \tag{48}$$

where $B^{(1)'} = B^{(1)}/U\omega^{-1}$ (49)

Substituting the expression for $u^{(1)'}$ into (47), the function $B^{(1)'}$ can then be solved numerically. The detailed solution procedures are described in Appendix B.

Equation (46) gives the longitudinal dispersion coefficient for the turbulent oscillatory pipe flows. The corresponding non-dimensional longitudinal dispersion coefficient can be expressed as,

$$D_l' = \frac{D_l}{Ua} = -\frac{\alpha}{\kappa} \frac{1}{(1-r_0')^2} \int_0^{1-r_0'} \text{Re}\left[u^{(1)'}B_*^{(1)'}\right]r'dr' \tag{50}$$

where the integral can be computed numerically as well.

Based on the above, the relationship between the non-dimensional longitudinal dispersion coefficient D_l' and the control parameter α is illustrated in Figure 6. A comparison is made between $\phi = 0.6$ and 1, the two values being chosen to approximate the range of ϕ. As before, r_0' is set to be 0.001 and 0.005. Figure 6 clearly shows that D_l' increases with α first and then slightly decreases with the peak at $\alpha \sim 20$. In addition, it can be observed from the figure that:

(i) keeping r_0' the same, D_l' is larger with larger ϕ when α is small, however, the situation reverses when α exceeds around 20, which can be attributed to the change-over of δ_I'. Moreover, a larger ϕ tends to have a lower peak value that appears at a relatively smaller α; and

(ii) keeping ϕ the same, D_l' is larger with larger r_0' when α is small. As α further increases, the two reach almost the same peak value. This is reasonable because the velocity profile is more uniform with larger α, and the significance of the velocity variation near the wall to the longitudinal dispersion diminishes.

For comparison, the cross-sectional averaged turbulent dispersivity $\langle D_t{'} \rangle$ is plotted in Figure 7. From the figure, $\langle D_t{'} \rangle$ increases with α first and then decreases, which can also be attributed to the change-over of $\delta_l{'}$ at $\alpha \sim 20$. Similarly, $\langle D_t{'} \rangle$ is higher with larger $r_0{'}$ but the $r_0{'}$ effect reduces when α exceeds the change-over point. $\langle D_t{'} \rangle$ also increases with ϕ proportionally as described in (29).

Comparing Figures 6 and 7, the difference between $D_l{'}$ and $\langle D_t{'} \rangle$ in turbulent flows varies considerably depending on the value of α. For most cases, $\langle D_t{'} \rangle$ is much smaller than $D_l{'}$. However, for $\alpha \sim O(0.1)$, the magnitude of $D_l{'}$ is of the same order as $\langle D_t{'} \rangle$, which implies that the turbulent dispersivity cannot be ignored in the analysis of the axial dispersion in oscillatory flows with small velocity amplitude but high frequency.

3. Experiments

3.1 Experimental apparatus and conditions

The experimental setup is shown in Figure 8. The experiments were conducted in a straight circular acrylic pipe with inner diameter $d = 10$mm and length $l = 1100$mm. One end of the pipe was connected to a water tank (250mm×250mm×500mm) with a valve installed on the entrance of the pipe. The other end was joined to a piston chamber with the inner diameter twice of the pipe diameter, i.e. 20mm. Both connections were equipped with bell-shaped transition to minimize the entrance effect. Flow oscillations were generated by a motor-and-crank assembly driving a low-friction stainless steel piston inside the piston chamber. A constant rotating speed was provided by an electric step motor, which was then converted to a sinusoidal movement in the horizontal direction to the piston through the Scotch-yoke

mechanism. The stroke volume (i.e. the flow displacement volume over a half period) V could be adjusted from 6.3 to 31.4 cm^3 by changing the length of the rotation arm and the frequency of the motor which ranged from 30 to 240 rpm.

According to the previous studies on the transition to turbulence of oscillatory pipe flows, the critical boundary Reynolds number for transition, Re_δ, was unanimously found to be around 500-550 [34-37], where Re_δ is defined by $\dfrac{U\delta}{\nu}$, $\delta = \sqrt{\dfrac{2\nu}{\omega}}$ is the Stokes layer thickness and ν the kinematic viscosity. In the present study, a total of 18 conditions were examined and their detailed experimental conditions are listed in Table 1 (the kinematic viscosity ν was ~10^{-6} m^2/s under the testing temperature 25$^\mathrm{o}$C). The experimental parameters included a range of Re_δ from 100 to 1000, with the intention of covering the oscillatory flow regime from laminar to turbulent.

3.1.1 Particle Image Velocimetry experiments

The kinematic characteristics of the oscillatory pipe flows in the experiments were first investigated using the laser-based Particle Image Velocimetry (PIV) technique. The working principle of PIV is straightforward. The flow field is first seeded with tracer particles and illuminated by dual-pulsing laser light sheets in regular frequency. Two short-duration exposures of the particles are recorded with the dual pulses on CCD camera correspondingly, with a carefully chosen pulse interval. The recorded dual images are then analyzed to obtain the instantaneous velocity map using cross-correlation algorithm with validations [38]. In the experiment, tap water was used as the working fluid, and 5μm neutral buoyant polyamid particles (density = 1.03 g/cm^3) were added as seeding particles. The light source employed

was a Dantec DualPower 50-100 Nd: YAG laser which could emit pulsed laser light with 532nm wavelength. A Dantec SpeedSense 1040 charge-coupled device (CCD) digital camera was configured for the image capturing with a filter lens of 532nm placed to eliminate other light sources. The laser sheet was adjusted to coincide with the pipe centerline section vertically while the camera was perpendicular to the plane illuminated by the laser. In this manner, the centerline velocities can be determined directly without the concern of refraction errors, while observations of the presence of eddies can also be made. An area of 10 mm (length) $\times$ 10 mm (height) in the middle of the pipe was chosen to be the image window. The distance from the measured area to the pipe ends was adequately long so that the entrance effect can be ignored. The frequency of the laser dual-pulses was set to be 20 times of the oscillation frequency of the flow for the determination of the centerline velocity, i.e. 20 pairs of images were captured within one oscillation period for each experimental condition. For the observation of cross-section eddies, a larger image window with lower sampling frequencies was adopted instead.

3.1.2 Planar Laser Induced Fluorescence experiments

The laser imaging technique of Planar Laser Induced Fluorescence (PLIF) was applied to quantify the longitudinal dispersion in the oscillatory pipe flows. PLIF measured the solute concentration by introducing an amount of dissolvable fluorescent dye into the fluid as tracer and then converting the dye image intensity to concentration through proper calibration [38]. The light source employed was a Dantec DualPower 65-15 Nd: YAG laser and the camera was a Dantec FlowSense 2M CCD digital camera. The tracer used in the present study was Rhodamine B (molecular diffusivity = 4.5×10^{-10} m^2/s [39]), which could emit fluorescent light with a peak wavelength of 575nm on excitation by the 532nm laser light. The dye

concentration was chosen in the linear range whereby the intensity of the fluorescent light was linearly proportional to the solute concentration. Hence, the concentration distribution along the pipe can be obtained by analyzing the fluorescent light intensity. A filter lens of 560nm was configured on the camera so that only the fluorescent light emitted by the excited tracer can be detected. A length of 350mm in the middle of the pipe was chosen to be the measurement section.

Due to the high sensitivity of PLIF, calibration was conducted before each test to determine the relationship between the light intensity and tracer concentration. Each calibration curve was obtained by detecting the light intensity of Rhodamine B solutions of five different concentrations, i.e. 20, 40, 60, 80 and 100 μg/L, and one blank sample. The precise concentration was obtained by a fluorometer. Single-frame mode was applied to capture the dispersion along time with the frequency of laser pulse being four times of the oscillation frequency. Each original image was then analyzed pixel by pixel based on the calibration curve to give the concentration distribution.

Different from the syringe-injected method in the literature which may induce injection momentum [22], the dye tracer was introduced to the fluid inside the pipe through the tank located at one end of the pipe. The dye solution was first mixed homogeneously inside the tank, which was separated with the tap water in the pipe initially by a valve at the entrance (see Figure 8) which was closed before the experiment. This method was preferred as it avoided introducing initial momentum to the tracer, as well as enabled the dye tracer to be homogeneous over the cross section before entering the pipe so that the influence of initial radial differences can be minimized. The solution concentration in the chamber was set to be around 80μg/L (the concentration was determined accurately by the fluorometer for each test).

3.2 Experimental results and analysis

3.2.1 Velocity measurements

Through the Scotch-yoke mechanism, which is a reciprocating motion mechanism where the reciprocating part is directly coupled to a sliding yoke with a slot that engages a pin on the rotating part, the constant-speed rotation of the motor could be converted to sinusoidal movements of the piston in the axial direction. Figure 9 shows the variation of phase-averaged axial velocity at the centerline of the pipe under different experimental conditions, where the symbols denote the measured velocities and the solid line represents the prediction from the present analytical analysis. The velocity applied is the non-dimensional velocity $u'(r'=0)$, i.e. $[u(r=0)]/U$, where $[\ ]$ represents the ensemble (phase) average over 100 cycles and U the amplitude of cross-sectional mean velocity. From the figure, it can be seen that the velocities followed well with the anticipated predictions.

Figure 10 shows the instantaneous velocity maps at different phases within a period under various Reynolds numbers, with the length of the vector representing the velocity amplitude and the arrow denoting the velocity direction (each velocity map was analyzed through peak validation, range validation and moving average validation to eliminate the incorrect vectors). Note that the velocity distribution was only indicative, as the refraction effect of the curvilinear pipe wall was not corrected. Clearly, the flow directions in the core region and near boundaries were opposite at the stage of flow reversal. This illustrated the existence of phase lag, whereby the flow near the wall boundaries switched direction earlier than the core region because of its velocity magnitude is smaller. In general, for small Reynolds numbers, the PIV velocity maps showed that the flows were smooth and unidirectional under most phases. However, disturbance can sometimes be observed when the flow changed direction

(i.e. Figure 10(a)), and these disturbance became more noticeable at larger Re_δ (i.e. Figure 10(b)). As Re_δ continued to increase, cross-sectional vortices began to appear around the phase of direction-change when Re_δ exceeded 501 (i.e. Figure 10(c)). The vortices were firstly observed in the domain between the core region and wall boundaries and gradually occupied the whole section as Re_δ further increased. The observation therefore implied that the oscillatory pipe flow transited from laminar to turbulent at some particular phases when Re_δ was ~500. Our observed value coincided with the reported critical boundary Reynolds number for transition to turbulence [34].

3.2.2 Concentration measurements

A complete longitudinal dispersion process within one oscillation period is qualitatively illustrated in Figure 11. Within the oscillation period, the solute moves forward and backward to the original position while diffuses/disperses at the same time. As the volume of Rhodamine B solution in the tank was much larger than the volume of tap water inside the pipe, the concentration in the tank can be treated approximately as a constant during the experiments for analysis. In the present study, the period of flow oscillation was less than 2 seconds while the time scales for dispersion along the pipe ranged from $O(10^2 s)$ to $O(10^6 s)$. The large contrast implied that the time scale for longitudinal dispersion was much longer compared to that of the flow oscillation. As a result, the analysis of the measurements can be performed similar to the transient constant-source diffusion/dispersion in an infinite pipe. Therefore, before the tracer reached the other end of the pipe, the concentration distribution would satisfy a complementary error function for a maintained source, which is:

$$C(x,t) = C_0 erfc\left(\frac{x}{2\sqrt{D_{eff}t}}\right) \qquad (51)$$

with the initial condition:

$$C(x,0) = 0 \qquad (52)$$

and the boundary conditions:

$$C(0,t) = C_0; C(\infty,t) = 0 \qquad (53)$$

where C_0 is the constant-source concentration and D_{eff} is the effective dispersion coefficient.

Figure 12 shows the concentration distribution according to the complementary error function qualitatively. By assuming the value of dispersion coefficient, one can obtain the quantitative concentration at any particular instance in time. In the present study, we analyzed the cross-sectional averaged concentration variation as a function of time at three different x positions, i.e. 0.46, 0.55 and 0.64m (note that the distortion induced by the cylindrical pipe wall was corrected). Through the fitting of the complementary error function to the experimental data, the best-fit longitudinal dispersion coefficient can be obtained for each condition.

The influence of the two independent parameters, i.e. stroke volume and oscillating frequency, on the longitudinal dispersion coefficient is demonstrated in Figure 13. In the figure, D_{eff}' is the non-dimensional dispersion coefficient defined by $\frac{D_{eff}}{D_{mol}}$, with D_{eff} employed for the calculation being the average value of the measured effective dispersion coefficient over the three x positions and D_{mol} is the molecular diffusivity of Rhodamine B ($D_{mol} = 4.5 \times 10^{-10}$ m^2/s). Under constant oscillating frequency, D_{eff}' increased with the non-

dimensional stroke volume $\dfrac{V^2}{a^6}$ as shown in Figure 13(a). A similar trend can be observed in

Figure 13(b) for a specific stroke volume. As the Womersley number $\sigma = a\sqrt{\omega/\nu}$ increased,

$D_{eff}{}'$ also increased generally.

The relationship between $D_{eff}{}'$ and Re_δ is further illustrated in Figure 14. As Re_δ increased

from 100 to 1000, the amplitude of $D_{eff}{}'$ increased from 10^3 to 10^7, implying that the

dimensional dispersion coefficient D_{eff} increased drastically from 10^{-6} to 10^{-2} m^2/s.

Comparing the dispersion coefficient with the same Reynolds number, D_{eff} was relatively

larger for the conditions with larger stroke volumes but smaller angular frequencies. In other

words, the oscillatory flow with smaller velocity amplitudes but longer periods introduced

stronger longitudinal dispersion than that with larger velocity amplitudes but shorter periods,

even though the two Reynolds number were identical. This is deemed reasonable as the

primary cause for longitudinal dispersion is the velocity variation over the cross section.

Oscillatory flows with higher velocity but shorter period have thinner boundary layers. Hence,

the velocity profile is flatter and thus weaker longitudinal dispersion is induced.

4. Comparison

According to the previous literature on the transition to turbulence in oscillatory pipe flows,

the oscillatory flow can be divided into three different regimes depending on the Reynolds

number Re_δ and the Stokes parameter λ ($\lambda = a\sqrt{\omega/(2\nu)}$) [34, 35]: (1) Laminar (and

distorted laminar) regime: the velocity distribution agrees with or distorts in part from the

laminar profile at low Reynolds numbers; (2) Transitional (or weakly turbulent) regime:

small amplitude perturbations are superposed on the distorted laminar flow at relatively high

Reynolds number; and (3) Turbulent (or conditional turbulence) regime: turbulence occurs in the decelerating phases when $\mathrm{Re}_\delta \geq$ 500-550. In the present study, the experimental conditions corresponded to the different regimes as follow: runs 1 and 2 (laminar), runs 3 – 10 (transitional) and runs 11 – 18 (turbulent). In the following, the experimental results are compared to the theoretical predictions based on previous laminar flow analysis and with the present analytical model, respectively.

4.1 Laminar flows

A classical theoretical study on the longitudinal dispersion coefficient of laminar pipe flows under sinusoidal pressure gradient was performed by Watson [6]. He concluded that the dispersion coefficient can be related to the stroke volume and angular frequency as follow:

$$D_{lam} = D_{mol}\left(1 + f(\sigma, Sc)\frac{V^2}{a^6}\right) \tag{54}$$

Figure 15 shows the ratio of the measured longitudinal dispersion coefficient D_{eff} to the theoretical prediction D_{lam} based on equation (54) as a function of Reynolds number. In the laminar regime, the measured dispersion coefficients were found to deviate from the Watson's theoretical predictions with the order of unity. The reason for this discrepancy might be the disturbances generated by the entrance. For Re_δ between 200 and 425, the measured values of the longitudinal dispersion coefficient became an order of magnitude higher than the laminar predictions, with the ratio $\dfrac{D_{eff}}{D_{lam}}$ ascending to O(10). As the Reynolds number increased, a drastic jump occurred when Re_δ exceeded ~ 500, as observed by the PIV velocity maps that the cross-sectional vortices began to appear. The presence of

turbulence now significantly enhanced the longitudinal dispersion coefficient, and the ratio $\dfrac{D_{eff}}{D_{lam}}$ increased to as large as $O(10^3)$ as a result.

4.2 Turbulent flows

With the analytical results in Section 2, the non-dimensional parameter α and the corresponding D_l' can be computed for each condition. The values of α for the 18 conditions were 3.2, 6.4, 9.6, 12.8 and 16, respectively. The comparison between the experimental results and the theoretical predictions for turbulent oscillatory flows as a function of Re_δ is illustrated in Figure 16, where $D_{tur} = D_l'Ua$ and D_l' is the non-dimensional turbulent dispersion coefficient under $r_0' = 0.001$ and $\phi = 1$ as expressed in equation (50). Clearly, for Re_δ less than 500, the predicted D_{tur} was much larger than D_{eff}, as the perturbation analysis is not applicable in the laminar and transitional regimes. When Re_δ reached 500 and beyond, the measured dispersion coefficient became similar to the predicted value, and $\dfrac{D_{eff}}{D_{tur}}$ was of the order $O(1)$, which demonstrated a satisfactory agreement in general. The agreement suggests that even though the present analytical model is based on the gross assumption of turbulent flow throughout the cross section, it can provide satisfying predictions for the longitudinal dispersion coefficient in this regime.

5. Conclusions

In the present study, the longitudinal dispersion of turbulent oscillatory pipe flows was investigated both analytically and experimentally. For the analytical analysis, an

axisymmetric co-axial model for the eddy viscosity is proposed based on the planar two-layer approach by Trowbridge and Madsen [27], and the homogenization approach is adopted for the multi-scale perturbation analysis. The results show that the non-dimensional longitudinal dispersion coefficient can be quantified by means of a control parameter α which is the ratio of the velocity amplitude to the angular frequency and pipe radius. Generally, the magnitude of the non-dimensional longitudinal dispersion coefficient is found to first increase with α and then decrease upon reaching a peak value of ~ 0.5 at $\alpha \sim 20-30$. The non-dimensional turbulent dispersivity follows a similar trend as D_l' but in a more moderate manner. Overall, the dimensional longitudinal dispersion coefficient of turbulent oscillatory flow $D_{tur} = D_l'Ua$ can be enhanced by increasing the velocity U while keeping the other two parameters, i.e. ω and a, unchanged.

An experimental study using PIV and PLIF techniques was also conducted to measure the longitudinal dispersion coefficient in oscillatory pipe flows under various oscillation frequency and stroke volume. The boundary Reynolds number covered a wide range from 100 to 1000, and thus the measurements enabled the examination of flow regimes from laminar to turbulent. The experimental results showed that when the Reynolds number increased, the dispersion coefficient rose drastically from 10^{-6} to 10^{-2} m^2/s. By comparing the dispersion coefficient under the same Re_δ, it was observed that the oscillatory flow with lower velocity amplitude but longer oscillation period generated relatively stronger longitudinal dispersion than that with higher velocity but shorter period. Finally, the predicted longitudinal dispersion coefficients based on our analytical analysis, i.e. equation (46), agreed satisfactorily with the experimental measurements when Re_δ exceeded 500, which is consistent with the reported critical Reynolds number for the transition to turbulence. The good agreement verified the applicability of the analytical approach in this study.

Acknowledgement

References

[1] Taylor, G., *Dispersion of soluble matter in solvent flowing slowly through a tube.* Proceedings of the Royal Society of London Series a-Mathematical and Physical Sciences, 1953. **219**(1137): p. 186-203.

[2] Taylor, G., The *dispersion of matter in turbulent flow through a pipe.* Proceedings of the Royal Society of London Series a-Mathematical and Physical Sciences, 1954. **223**(1155): p. 446-468.

[3] Fischer, H. B., List, E. J., Koh, R. C. Y., Imberger, J. and Brooks, N, H., *Mixing in inland and coastal waters* 1979: Academic Press.

[4] Aris, R., *On the dispersion of a solute in pulsating flow through a tube.* Proceedings of the Royal Society of London Series a-Mathematical and Physical Sciences, 1960. **259**(1298): p. 370-376.

[5] Chatwin, P.C., *Longitudinal dispersion of passive contaminant in oscillatory flows in tubes.* Journal of Fluid Mechanics, 1975. **71**(OCT14): p. 513-527.

[6] Watson, E.J., *Diffusion in oscillatory pipe-flow.* Journal of Fluid Mechanics, 1983. **133**(AUG): p. 233-244.

[7] Mukherjee, A. and Mazumder, B.S., *Dispersion of contaminat in oscillatory flows.* Acta Mechanica, 1988. **74**(1-4): p. 107-122.

[8] Joshi, C.H., Kamm, R.D., Dragen, J.M. and Slutsky, A.S., *An experiment study of gas exchange in laminar oscillatory flow.* Journal of Fluid Mechanics, 1983. **133**: p. 245-254.

[9] Pedley, T. J. and Kamm, R. D., *The effect of secondary motion on axial transport in oscillatory tube flow.* Journal of Fluid Mechanics, 1988. **193**: p. 347-367.

[10] Ng, C.O., *Dispersion in steady and oscillatory flows through a tube with reversible and irreversible wall reactions.* Proceedings of the Royal Society a-Mathematical Physical and Engineering Sciences, 2006. **462**(2066): p. 481-515.

[11] Jiang, Y.H. and Grotberg, J. B., *Bolus contaminant dispersion in oscillatory tube flow with conductive walls.* Journal of Biomechanical Engineering-Transactions of the Asme, 1993. **115**(4): p. 424-431.

[12] Mazumder, B. S. and Das, S. K., *Effect of boundary reaction on solute-dispersion in pulsatile flow through a tube*. Journal of Fluid Mechanics, 1992. **239**: p. 523-549.

[13] Mazumder, B. S. and Paul, S., *Dispersion of reactive species with reversible and irreversible wall reactions*. Heat and Mass Transfer, 2012. **48**(6): p. 933-944.

[14] Sharp, M.K., Kamm, R. D., Shapiro, A. H., Kimmel, E. and Karniadakis, G. E., *Dispersion in a curved tube during oscillatory flow.* Journal of Fluid Mechanics, 1991. **223**: p. 537-563.

[15] Eckmann, D. M., *Bolus contaminant dispersion in oscillating flow in curved tubes.* Journal of Biomechanical Engineering-Transactions of the ASME, 1998. **120**: p. 238-244.

[16] Jayaraman, G., Pedley, T. J. and Goyal, A., *Dispersion of solute in a fluid flowing through a curved tube with absorbing walls*. Q. J. of Mechanics and Applied Mathematics, 1998. **51**: p. 577-598.

[17] Paul, S. and Mazumder, B. S., *Effects of nonlinear chemical reactions on the transport coefficients associated with steady and oscillatory flows through a tube*. Int. J. of Heat and Mass Transfer, 2011. **54**: p. 75-85.

[18] Ye, X. F. and Shimizu, M., *Augmented longitudinal diffusion in grooved tubes for oscillatory flow*. International Journal of Heat and Mass Transfer, 2001. **44**: p. 633-644.

[19] Mei, C. C., Liu, Y. H. and Law, A. W. K., *Theory of isobaric pressure exchanger for desalination.* Desalination and Water Treatment, 2012. **39**(1-3): p. 112-122.

[20] Mondal, K. K. and Mazumder, B. S., *Dispersion of fine settling particles from an elevated source in an oscillatory turbulent flow*. European Journal of Mechanics-B/Fluids, 2008. **27**: p. 707-725.

[21] Lee, J. S., *The mixing and axial transport of smoke in oscillatory tube flows*. Ann. Biomed. Eng., 1984. **12**: p. 371-383.

[22] Ye, X. F. and Zhang, J. W., *Effect of turbulence on Taylor dispersion for oscillatory flows.* International Journal of Heat and Mass Transfer, 2002. **45**: p. 4373-4380.

[23] Zhou, Y.H., Ding, X. W., Ju, M. W. and Chang, Y. Q., *Numerical simulation on a dynamic mixing process in ducts of a rotary pressure exchanger for SWRO.* Desalination and Water Treatment, 2009. **1**(1-3): p. 107-113.

[24] Liu, Y., Zhou, Y. H. and Bi, M. S., *3D numerical simulation on mixing process in ducts of rotary pressure exchanger.* Desalination and Water Treatment, 2012. **42**(1-3): p. 269-273.

[25] Mei, C. C. and Chian, C. M., *Dispersion of small suspended particles in a wave boundary layer.* Journal of Physical Oceanography, 1994. **24**: p. 2479-2495.

[26] Ng, C. O. and Wu, C. H., *Dispersion of suspended particles in a wave boundary layer over a viscoelastic bed*. International Journal of Engineering Science, 2008. **46**: p. 50-65.

[27] Trowbridge, J. and Madsen, O.S., *Turbulent wave boundary layer: 1. Model formulation and 1st-order solution.* J. Geophys. Res., 1984a. **89**: p. 7989-7997.

[28] Trowbridge, J. and Madsen, O.S., *Turbulent wave boundary layer: 2. 2nd-order theory and mass transpot.* J. Geophys. Res., 1984b. **89**: p. 7999-8007.

[29] Ng, C. O., *A time-varying diffusivity model for shear dispersion in oscillatory channel flow*. Fluid Dynamics Research, 2004. **34**: p. 335–355.

[30] Mazumder, B. S. and Paul, S., *Dispersion of settling particles in oscillatory turbulent flow subject to deposition and re-entrainment.* European Journal of Mechanics-B/Fluids, 2012. **31**: p. 80-90.

[31] Mei, C.C. and Vernescu, B., *Homogenization methods for multiscale mechanics* 2010: World Scientific publishing Co. Pte. Ltd.

[32] Fox, R.O., *Computational Models for Turbulent Reacting Flows*. Cambridge: Cambridge University Press, 2003. p. 438.

[33] Law, A.W.K., *Velocity and concentration distribution of round and plane turbulent jets.* Journal of Engineering Mathematics, 2006. **56**(1): p. 69-78.

[34] Hino, M., Sawamoto, M. and Takasu, S., *Experiments on transition to turbulence in an oscillatory pipe flow*. Journal of Fluid Mechanics, 1976. **75**: p. 193-207.

[35] Ohmi, M., Iguchi, M., Kakehachi, K. and Masuda, T., *Transition to turbulence and velocity distrubution in an oscillating pipe flow.* Bull. Japan Soc. Mech. Engrs., 1982. **25**: p. 365-371.

[36] Ahn, K.H. and Ibrahim, M.B., *Laminar/turbulent oscillating flow in circular pipes.* International Journal of Heat and Fluid Flow, 1992. **13**: p. 340-346.

[37] Akhaven, R., Kamm, R.D. and Shapiro, A.H., *An investigation of transition to turbulence in bounded oscillatory Stokes flows Part 1. Experiments.* Journal of Fluid Mechanics, 1991. **225**: p. 395-422.

[38] Law, A.W.K. and Wang, H.W., *Measurement of mixing processes with combined digital particle image velocimetry and planar laser induced fluorescence.* Experimental Thermal and Fluid Science, 2000. **22**(3-4): p. 213-229.

[39] Kapusta, P., *Absolute diffusion coefficient: compilation of reference data for FCS calibration.* PicoQuant GmbH, July 2010, Rev 1.

Appendix A. The auxiliary functions $F^{(n)}$

The solutions of the auxiliary functions are presented in this appendix. Recall the governing equation (17). Inside the inner boundary layer, $r_0' < s' \le \delta_I'$, we can assume $\frac{1}{1-s'} = 1 + s' + s'^2 \to 1$. Thus, (17) can be simplified as,

$$-inF^{(n)} + \alpha \overline{u_f}' \frac{d}{ds'} \left((1-s')s' \frac{dF^{(n)}}{ds'} \right) = 0 \tag{A 1}$$

The solution of (A 1) can be obtained as (note that one of the constants presented below is set to be one due to the fact that the equation (17) is homogeneous):

$$F^{(n)} = x_1 H \left(\left[\varphi^n, \varphi^n \right], \left[2\varphi^n \right], \frac{1}{s'} \right) s'^{-\varphi^n} + x_2 H \left(\left[\psi^n, \psi^n \right], \left[2\psi^n \right], \frac{1}{s'} \right) s'^{-\psi^n} \tag{A 2}$$

where H denotes the hypergeomatric functions and

$$\varphi^n = \frac{1}{2} - \sqrt{\frac{-in}{\alpha \overline{u_f}'} + \frac{1}{4}} \tag{A 3}$$

$$\psi^n = \frac{1}{2} + \sqrt{\frac{-in}{\alpha \overline{u_f}'} + \frac{1}{4}} \tag{A 4}$$

Outside the inner boundary layer and in the outer region, $\delta_I' \le s' \le 1$, equation (17) becomes,

$$-inF^{(n)} + \frac{\alpha \overline{u_f}' \delta_I'}{1-s'} \frac{d}{ds'} \left((1-s') \frac{dF^{(n)}}{ds'} \right) = 0 \tag{A 5}$$

The solution of $F^{(n)}$ in equation (A 5) can be obtained as,

$$F^{(n)} = x_2 J_0 \left(\gamma^n (s'-1) \right) + x_3 K_0 \left(-i\gamma^n (s'-1) \right) \tag{A 6}$$

where J_0 and K_0 represent the first and second kind Bessel function of order zero, respectively, and

$$\gamma^n = \sqrt{\frac{-in}{\alpha \overline{u_f}' \delta_I'}} \tag{A 7}$$

The unknown constants, x_1, x_2 and x_3, can be determined by applying the matching and boundary conditions (18a), (18b) and (19).

Appendix B. Solution of function $B^{(1)'}$

The solution procedures of function $B^{(1)'}$ are presented in this appendix. Recall that the governing equation is given in (47) and the boundary conditions in (48).

When $r_0' < s' < \delta_I'$, (47) becomes,

$$\phi \alpha \overline{u_f}' \frac{d}{ds'}\left((1-s')s'\frac{dB^{(1)'}}{ds'}\right) - iB^{(1)'} = i\left(\frac{F^{(1)}}{F^{(1)}(r_0')} - 1\right) + \frac{ia^{(2)}}{4}\left(\frac{F_*^{(1)}}{F_*^{(1)}(r_0')} - \frac{F^{(1)}}{F^{(1)}(r_0')}\right) \tag{B 1}$$

where $F^{(1)}$ is expressed by equation (A 2).

When $\delta_I' < s' < 1$, the governing equation is modified to,

$$\frac{\phi \alpha \overline{u_f}' \delta_I'}{1-s'} \frac{d}{ds'}\left((1-s')\frac{dB^{(1)'}}{ds'}\right) - iB^{(1)'} = i\left(\frac{F^{(1)}}{F^{(1)}(r_0')} - 1\right) + \frac{ia^{(2)}}{4}\left(\frac{F_*^{(1)}}{F_*^{(1)}(r_0')} - \frac{F^{(1)}}{F^{(1)}(r_0')}\right) \tag{B 2}$$

where $F^{(1)}$ is in the form of (A 6).

Discretizing with the second order central difference scheme, we have

$$y_x' = \frac{y_{x+1} - y_{x-1}}{2\Delta x}, \quad y_x'' = \frac{y_{x+1} - 2y_x + y_{x-1}}{\Delta x^2} \tag{B 3}$$

where y_x' and y_x'' represent the first and second order derivative of function y at x, respectively.

Let $y = B^{(1)'}$, $y' = \frac{dB^{(1)'}}{ds'}$ and $y'' = \frac{d^2 B^{(1)'}}{ds'^2}$, equations (B 1) and (B 2) can be written in the numerical form respectively as,

$$\left(-\Delta x + 2x\Delta x + 2x - 2x^2\right)y_{x-1} + \left(-4x + 4x^2 - \frac{2\Delta x^2}{\phi \alpha \overline{u_f}'}i\right)y_x + \left(\Delta x - 2x\Delta x + 2x - 2x^2\right)y_{x+1}$$

$$= \frac{2i\Delta x^2}{\phi\overline{\alpha u_f}'}\left(\left(\frac{F^{(1)}}{F^{(1)}(r_0')}-1\right)+\frac{a^{(2)}}{4}\left(\frac{F_*^{(1)}}{F_*^{(1)}(r_0')}-\frac{F^{(1)}}{F^{(1)}(r_0')}\right)\right) \tag{B 4}$$

$$(2-2x+\Delta x)y_{x-1}+\left(-4+4x-\frac{2\Delta x^2(1-x)}{\phi\overline{\alpha u_f}'\delta_I'}i\right)y_x+(2-2x-\Delta x)y_{x+1}$$

$$= \frac{2\Delta x^2(1-x)i}{\phi\overline{\alpha u_f}'\delta_I'}\left(\left(\frac{F^{(1)}}{F^{(1)}(r_0')}-1\right)+\frac{a^{(2)}}{4}\left(\frac{F_*^{(1)}}{F_*^{(1)}(r_0')}-\frac{F^{(1)}}{F^{(1)}(r_0')}\right)\right) \tag{B 5}$$

Denoting the coefficients of y_{x-1}, y_x, and y_{x+1} as Z, X and Y, respectively, and the RHS

as f, a matrix equation can be obtained as,

$$\begin{bmatrix} 1 & -1 & 0 & ... & 0 \\ Z_1 & X_1 & Y_1 & ... & 0 \\ & & & & \\ 0 & ... & Z_{m-1} & X_{m-1} & Y_{m-1} \\ 0 & ... & 0 & -1 & 1 \end{bmatrix} \times \begin{bmatrix} y_0 \\ y_1 \\ : \\ y_{m-1} \\ y_m \end{bmatrix} = \begin{bmatrix} 0 \\ f_1 \\ : \\ f_{m-1} \\ 0 \end{bmatrix} \tag{B 6}$$

The first and last rows represent the boundary conditions.

For the presentation of results, m was set to be 1000 typically.

FIGURE 8 – Experimental setup (unit: mm)

FIGURE 9 – Velocity variation at the centerline under different conditions. The solid lines represent the predictions based on equations (20) and (21), and the symbols denote the measured velocities

FIGURE 10 – Velocity vector maps under different conditions (unit: mm)

FIGURE 11 – Longitudinal dispersion process within one cycle for $\mathrm{Re}_\delta = 425$ ($V = 18.8$ cm^3, $\omega = 2\pi$ rad/s)

FIGURE 12 – Concentration distribution as a function of distance from a maintained source based on complementary error function

FIGURE 13 – Variation of measured non-dimensional longitudinal dispersion coefficient with (a) non-dimensional stroke volume and (b) Womersley number

FIGURE 14 – Relationship between measured non-dimensional longitudinal dispersion coefficient and Reynolds number

FIGURE 15 – Comparison between experimental results and theoretical predictions for laminar flows based on equation (54)

FIGURE 16 – Comparison between experimental results and theoretical predictions for turbulent flows based on equation (46)
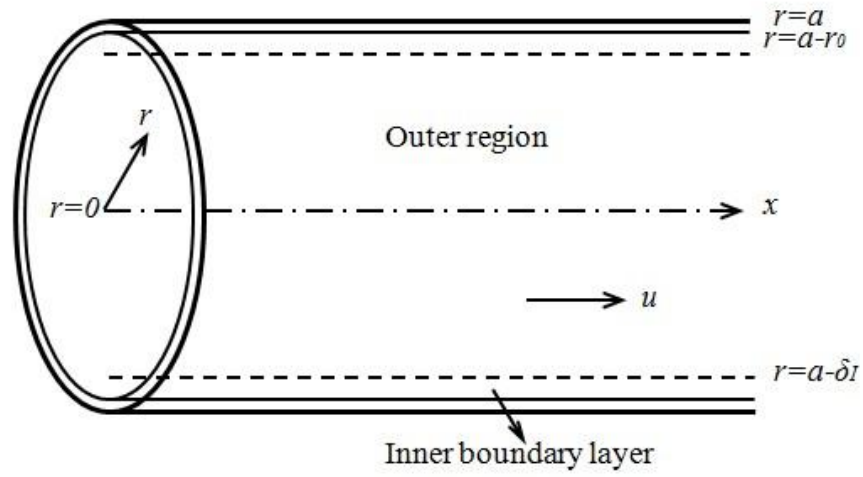
FIGURE 1. Schematic diagram of the coordinate axis for analysis
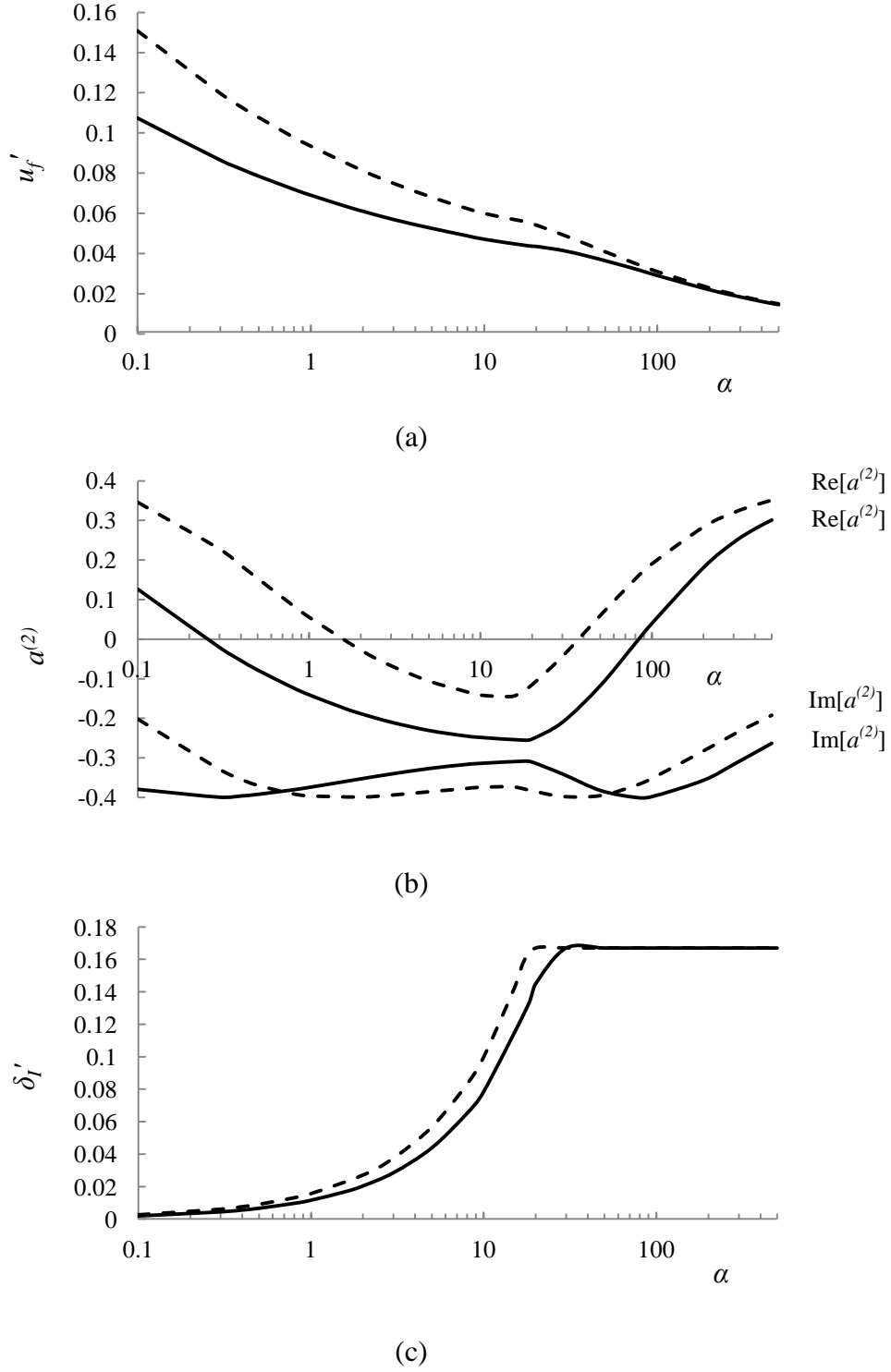
FIGURE 2. Variations of (a) friction velocity $\overline{u_f}{}'$ (equation (24)), (b) complex constant $a^{(2)}$ (equation (26)), and (c) inner boundary layer thickness $\delta_I{}'$ (equation (13)) with α. The solid curves are for $r_0{}' = 0.001$ and dashed curves for $r_0{}' = 0.005$
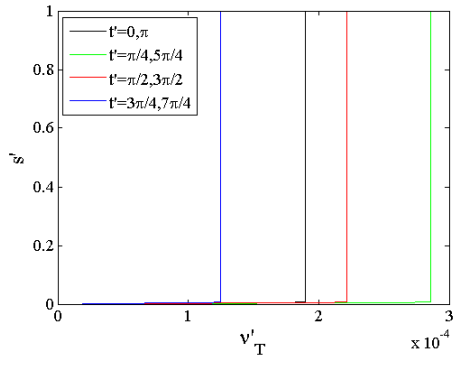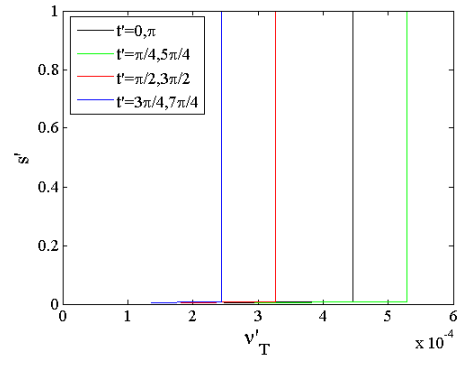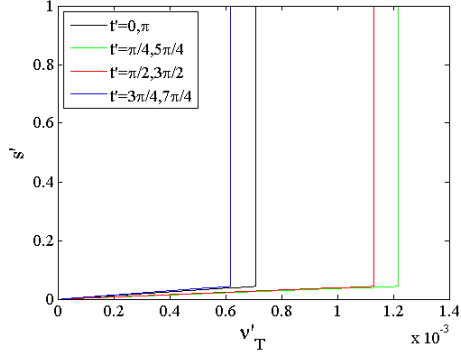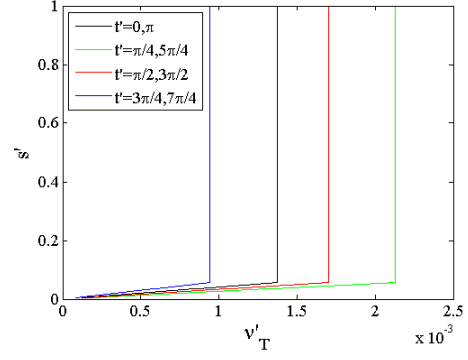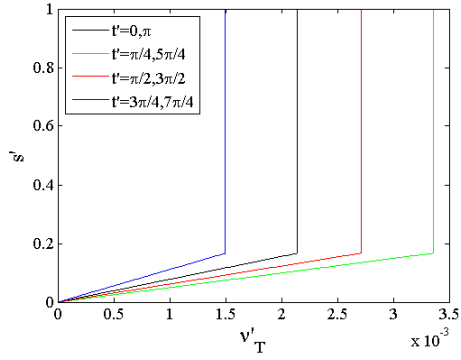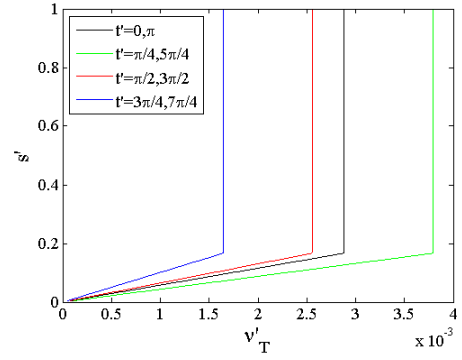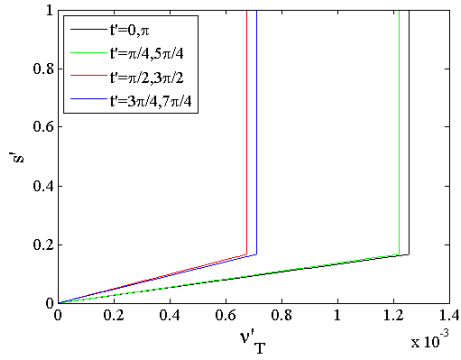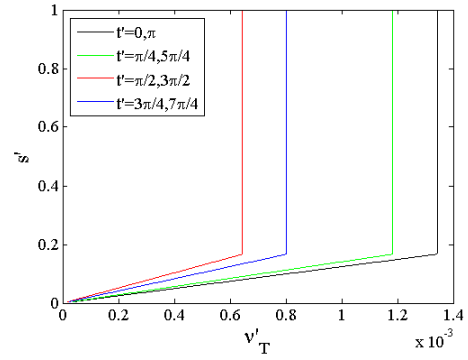
FIGURE 3. Profiles of eddy viscosity v_T' at various phases within the same period (left: $r_0' = 0.001$: (a) $\alpha = 0.5$, (b) $\alpha = 5$, (c) $\alpha = 50$, (d) $\alpha = 500$; right: $r_0' = 0.005$:(e) $\alpha = 0.5$, (f) $\alpha = 5$, (g) $\alpha = 50$, (h) $\alpha = 500$)
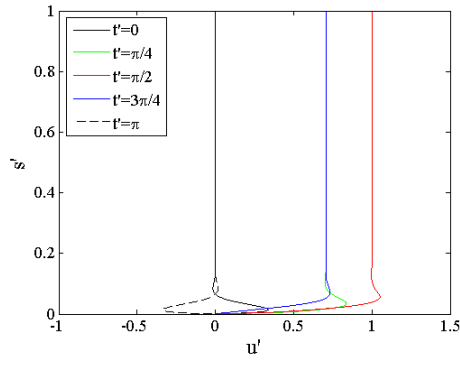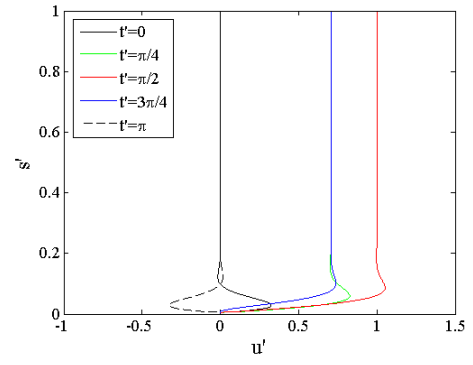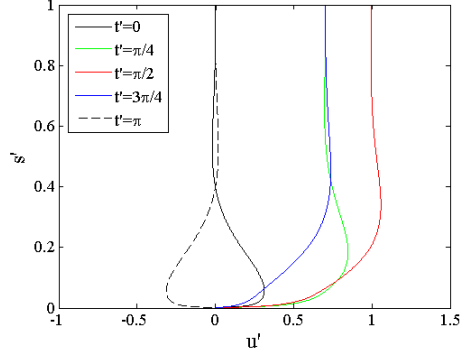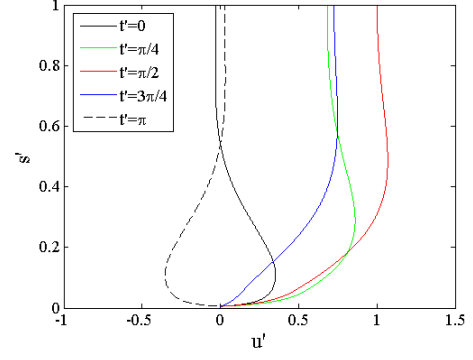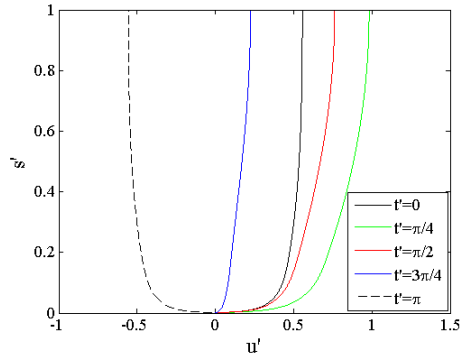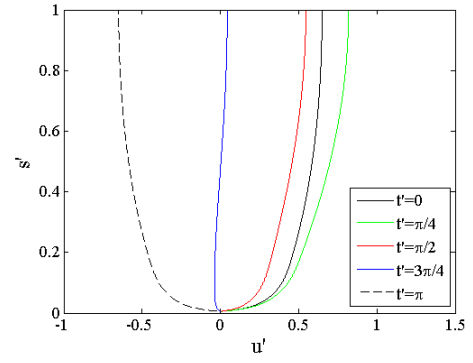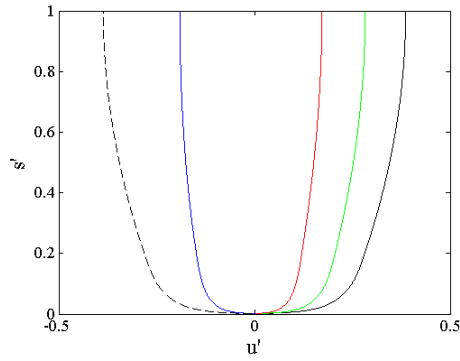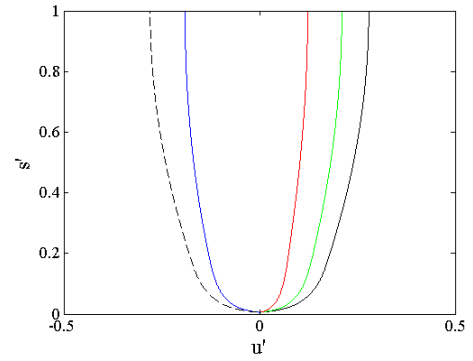
FIGURE 4. Profiles of velocity u' at various phases within the same period (left: $r_0' = 0.001$: (a) $\alpha = 0.5$, (b) $\alpha = 5$, (c) $\alpha = 50$, (d) $\alpha = 500$; right: $r_0' = 0.005$: (e) $\alpha = 0.5$, (f) $\alpha = 5$, (g) $\alpha = 50$, (h) $\alpha = 500$)
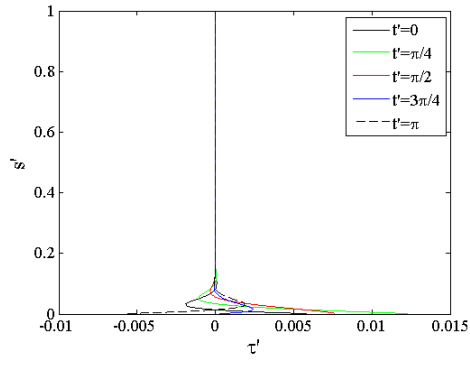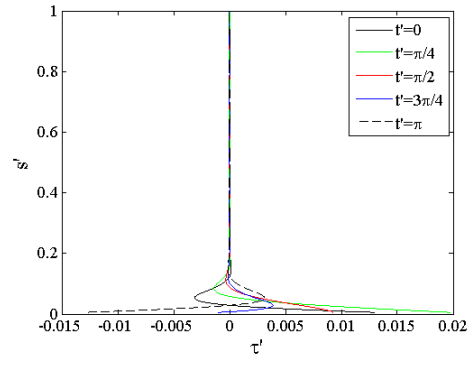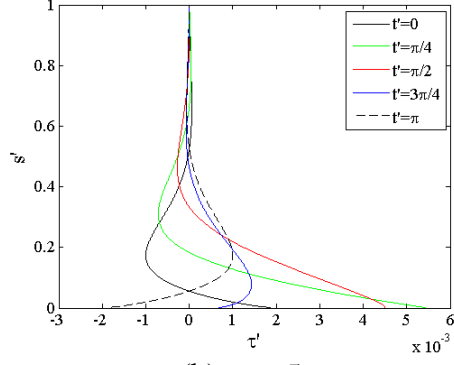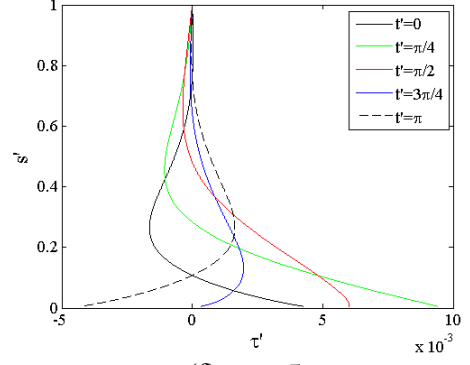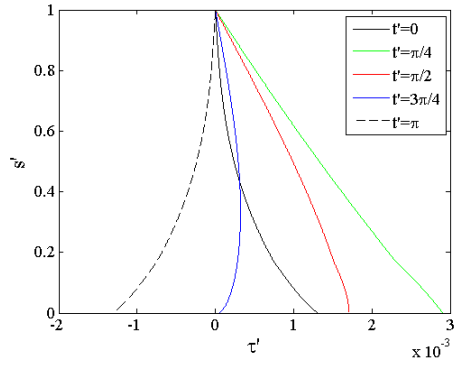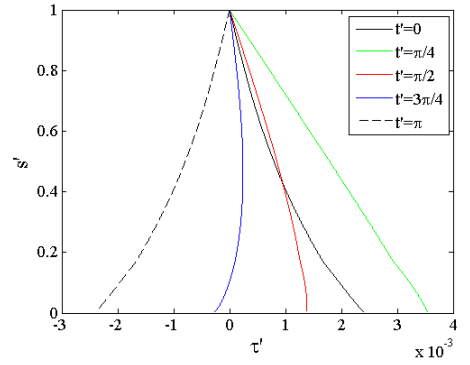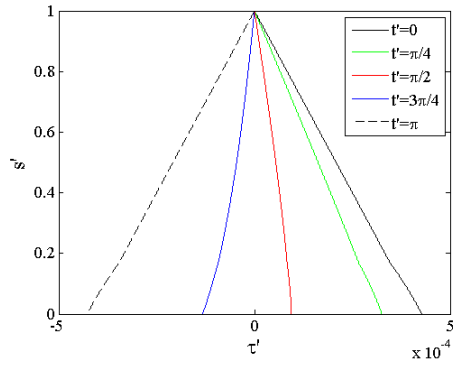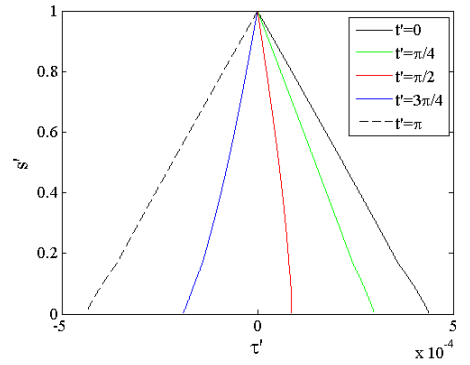
FIGURE 5. Profiles of shear stress τ' at various phases within the same period (left: $r_0' = 0.001$: (a) $\alpha = 0.5$, (b) $\alpha = 5$, (c) $\alpha = 50$, (d) $\alpha = 500$; right: $r_0' = 0.005$:(e) $\alpha = 0.5$, (f) $\alpha = 5$, (g) $\alpha = 50$, (h) $\alpha = 500$)
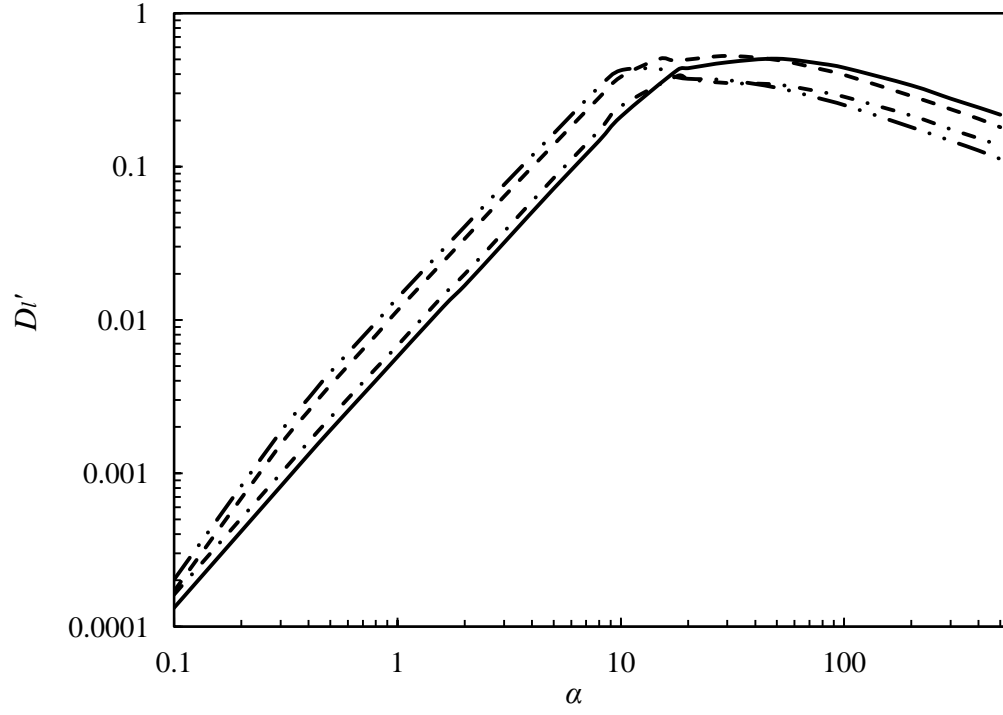
FIGURE 6. The non-dimensional turbulent longitudinal dispersion coefficient D_l' based on equation (50) as functions of α with $\phi = 0.6, r_0' = 0.001$ (solid), $\phi = 0.6, r_0' = 0.005$ (dash), $\phi = 1, r_0' = 0.001$ (dash dot), and $\phi = 1, r_0' = 0.005$ (dash dot dot)
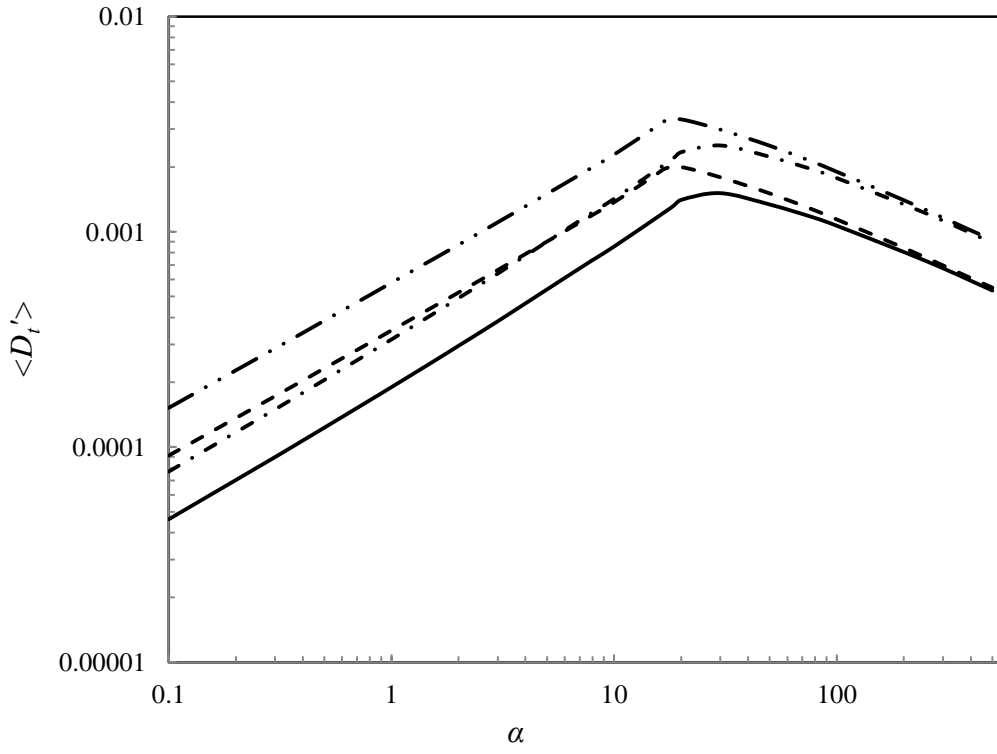
FIGURE 7. The non-dimensional turbulent dispersivity $\langle D_t ' \rangle$ as functions of α with

$\phi = 0.6, r_0 ' = 0.001$ (solid), $\phi = 0.6, r_0 ' = 0.005$ (dash), $\phi = 1, r_0 ' = 0.001$ (dash dot), and

$\phi = 1, r_0 ' = 0.005$ (dash dot dot)
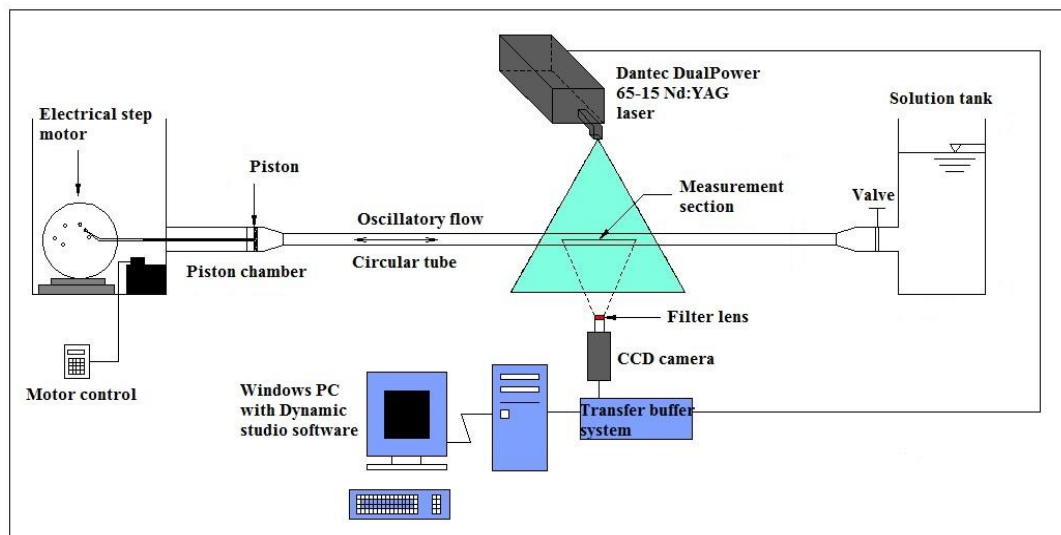
FIGURE 8. Experimental setup (unit: mm)
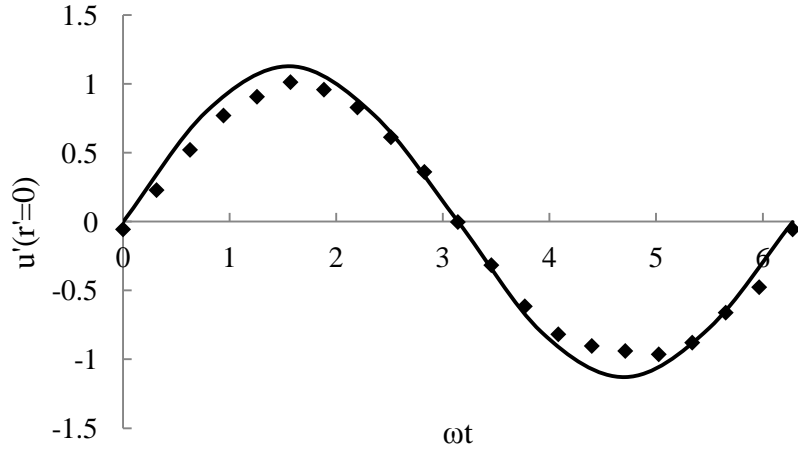
(a) $\mathrm{Re}_\delta = 802$ ($V = 25.1\,\mathrm{cm}^3$, $\omega = 4\pi\,\mathrm{rad/s}$)
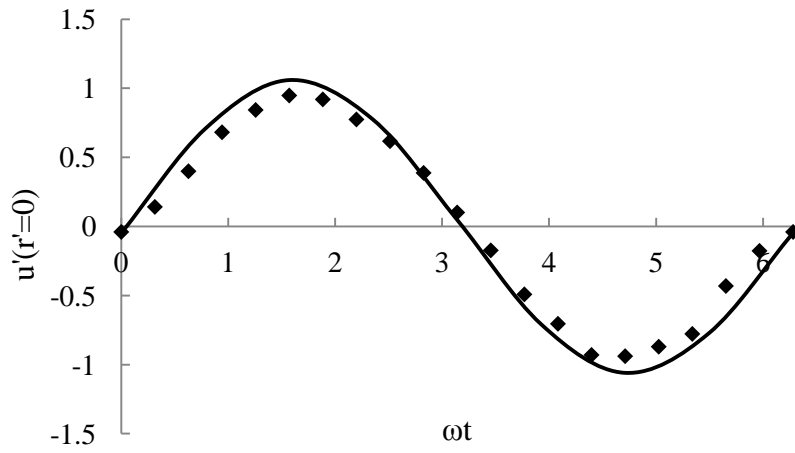
(b) $\mathrm{Re}_\delta = 850$ ($V = 18.8\,\mathrm{cm}^3$, $\omega = 8\pi\,\mathrm{rad/s}$)
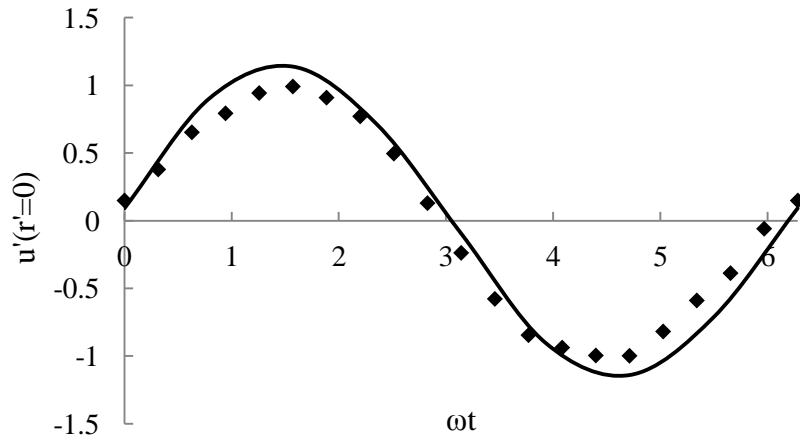
(c) $\mathrm{Re}_\delta = 1002$ ($V = 31.4\,\mathrm{cm}^3$, $\omega = 4\pi\,\mathrm{rad/s}$)

FIGURE 9. Velocity variation at the centerline under different conditions. The solid lines represent the predictions based on equations (20) and (21), and the symbols denote the measured velocities.
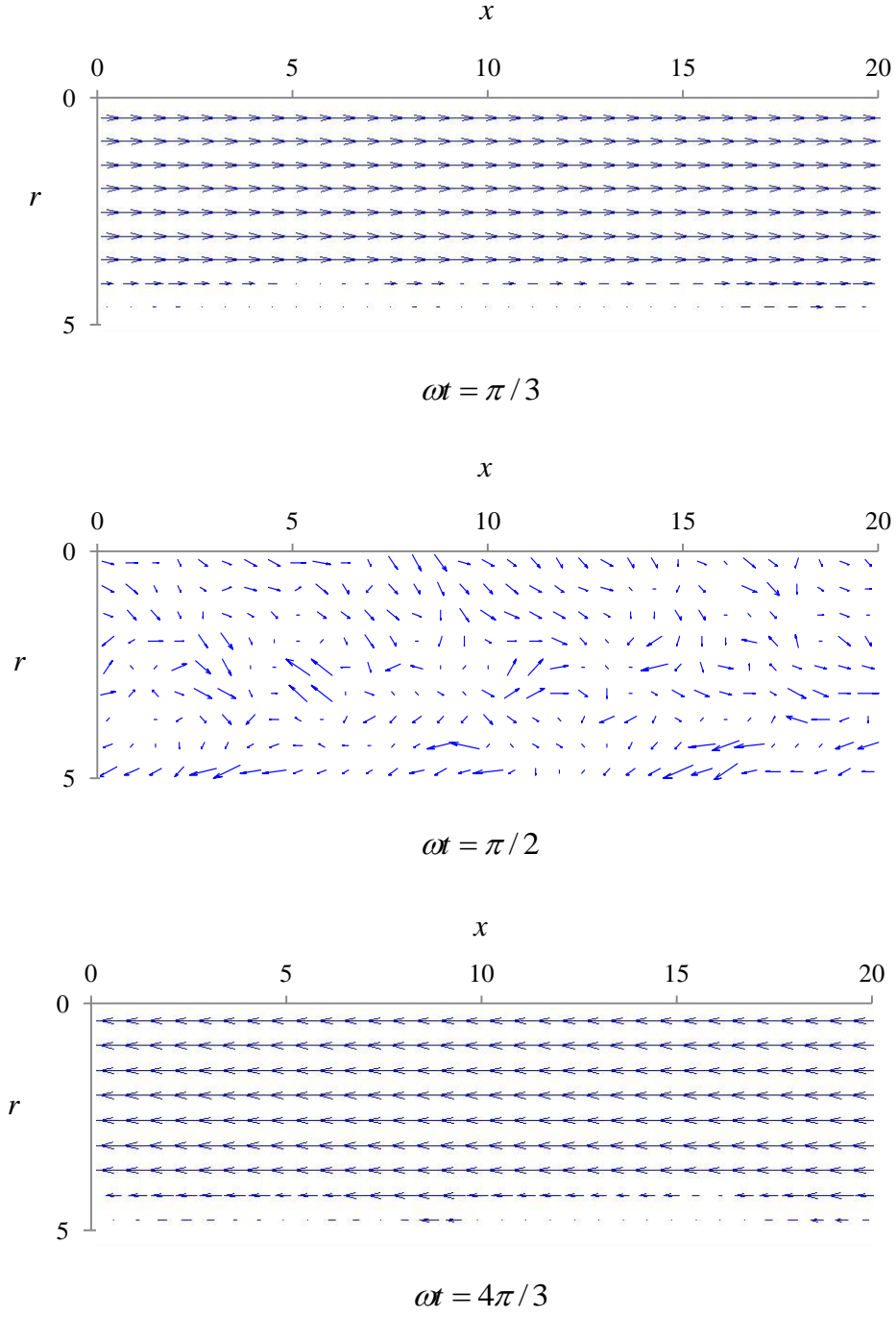
51
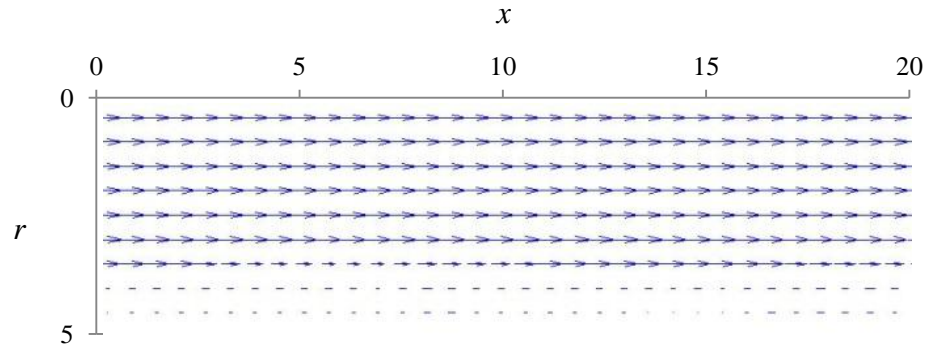
$$\omega t = \pi / 3$$
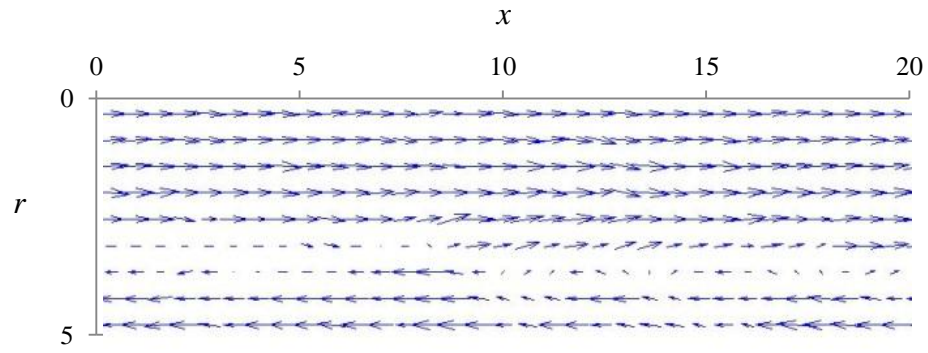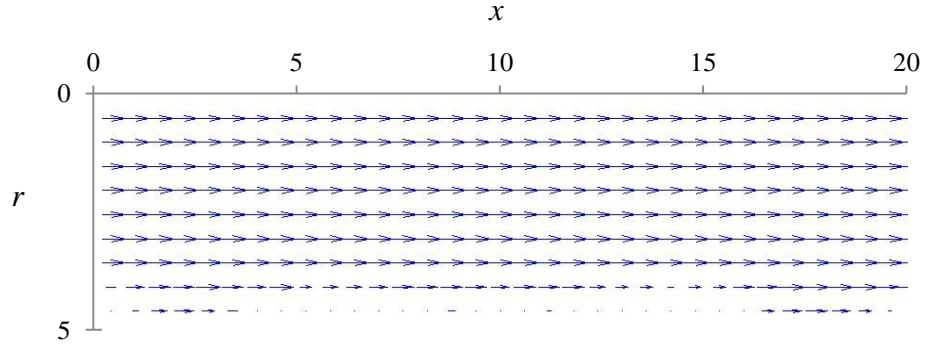

$$\omega t = \pi / 2$$
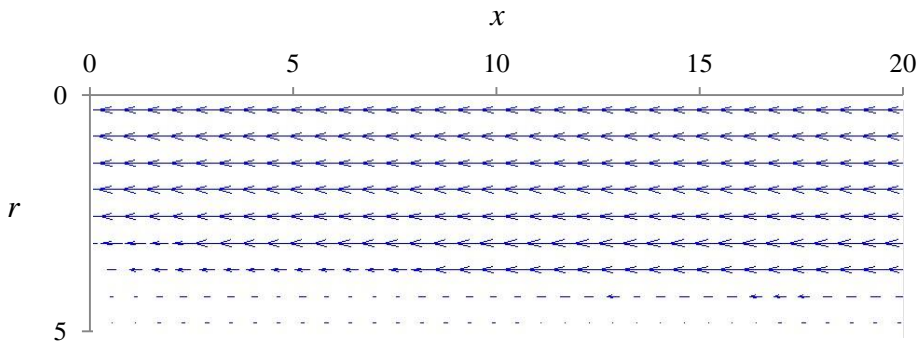
$$\omega t = 4\pi / 3$$

(a) $\mathrm{Re}_\delta = 200$ ($V = 12.6\,\mathrm{cm}^3$, $\omega = \pi\,\mathrm{rad/s}$)

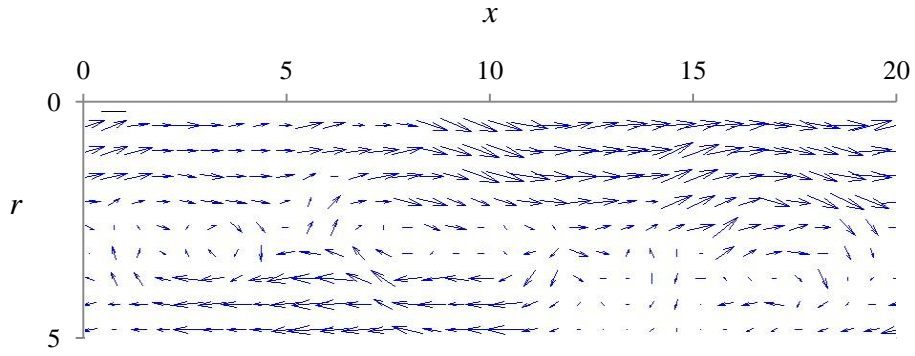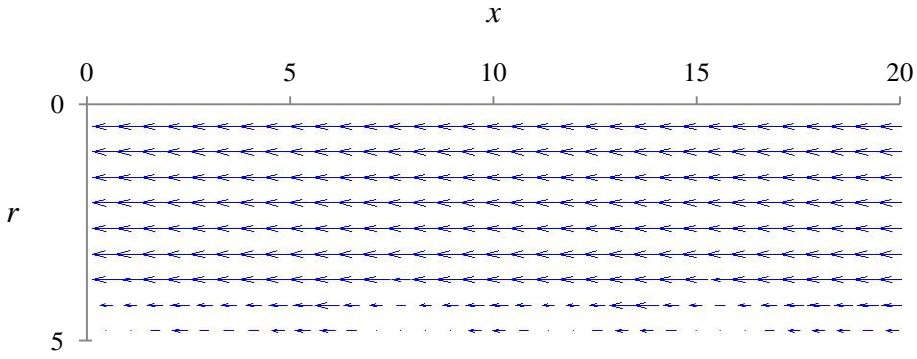FIGURE 10. Velocity vector maps under different conditions (unit: mm)

$$\omega t = \pi / 3$$

$$\omega t = \pi / 2$$

$$\omega t = 4\pi / 3$$

(b) $\mathrm{Re}_{\delta} = 283$ ($V = 12.6\,\mathrm{cm}^3$, $\omega = 2\pi\,\mathrm{rad/s}$)

FIGURE 10. Velocity vector maps under different conditions (unit: mm) (continued)

$$\omega t = \pi / 3$$

$$\omega t = \pi / 2$$

$$\omega t = 4\pi / 3$$

(c) $\mathrm{Re}_\delta = 567$ ($V = 25.1\,\mathrm{cm}^3$, $\omega = 2\pi\,\mathrm{rad/s}$)

FIGURE 10. Velocity vector maps under different conditions (unit: mm) (continued)

$\omega t = 0$

$\omega t = \pi / 6$

$\omega t = \pi / 3$

$\omega t = \pi / 2$

$\omega t = 2\pi / 3$

$\omega t = 5\pi / 6$

$\omega t = \pi$

$\omega t = 7\pi / 6$

$\omega t = 4\pi / 3$

$\omega t = 3\pi / 2$

$\omega t = 5\pi / 3$

$\omega t = 11\pi / 6$

$\omega t = 2\pi$
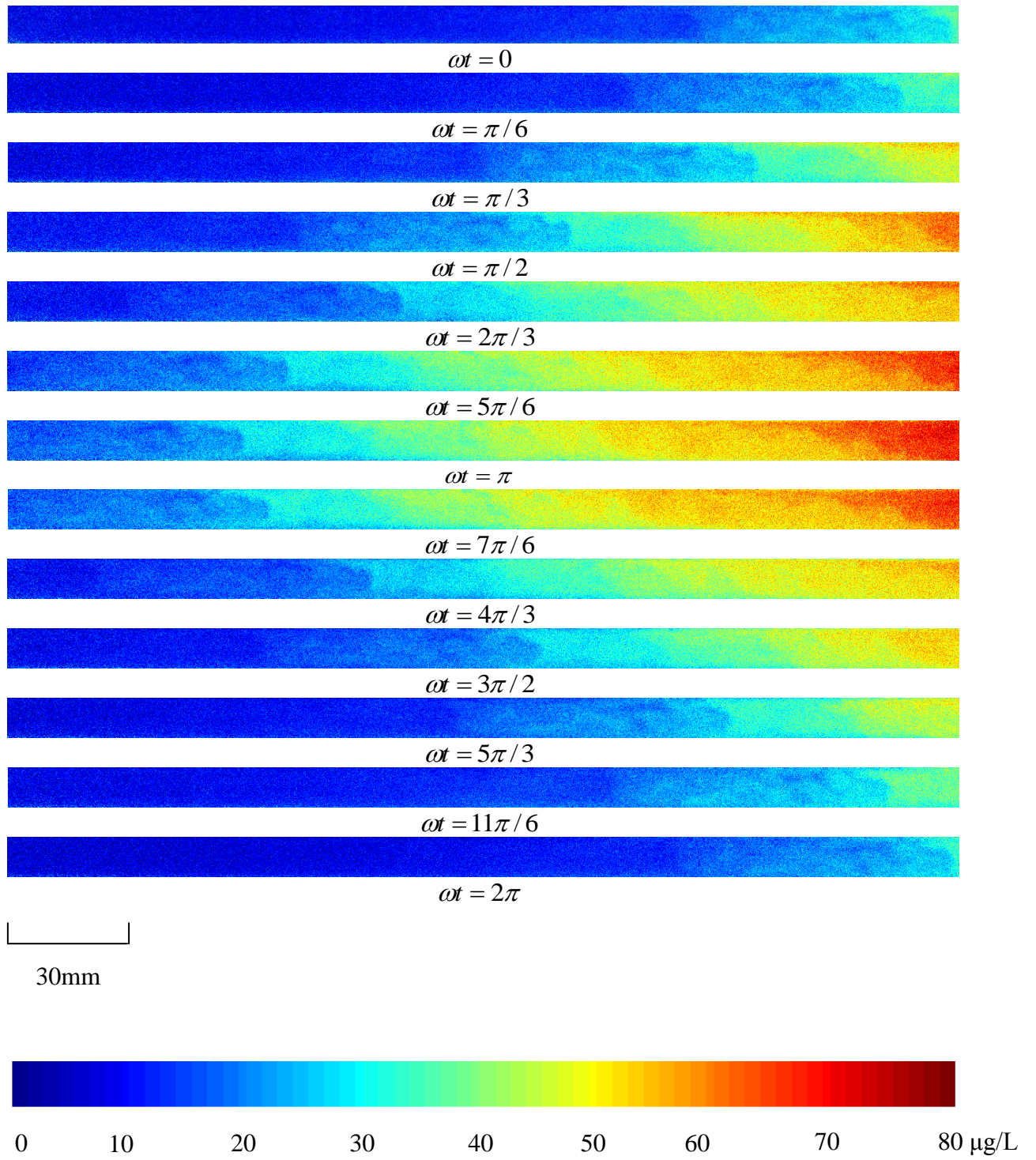
30mm

| 0 | 10 | 20 | 30 | 40 | 50 | 60 | 70 | 80 µg/L |

FIGURE 11. Longitudinal dispersion process within one cycle for $\text{Re}_\delta = 425$

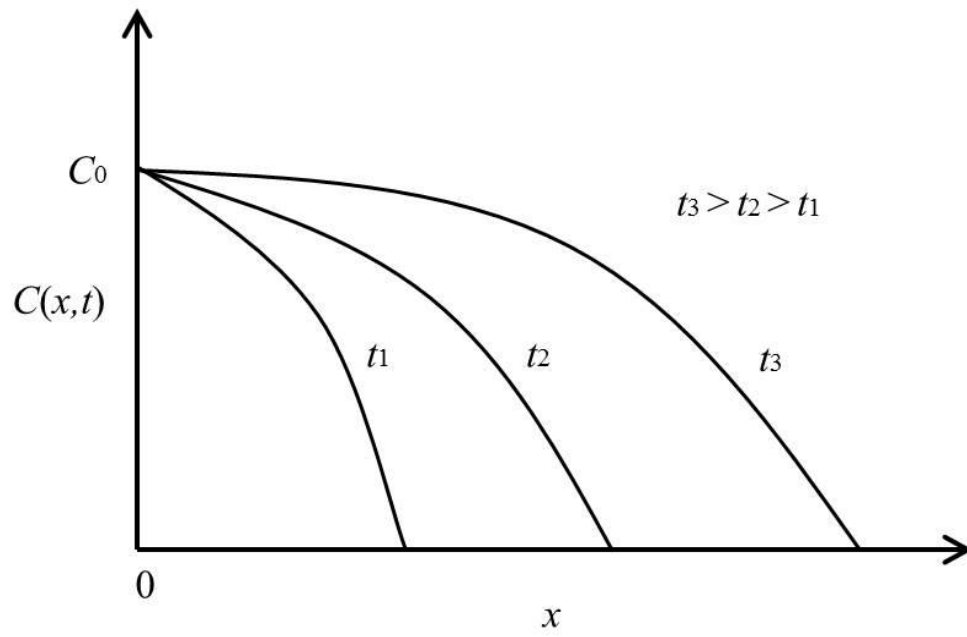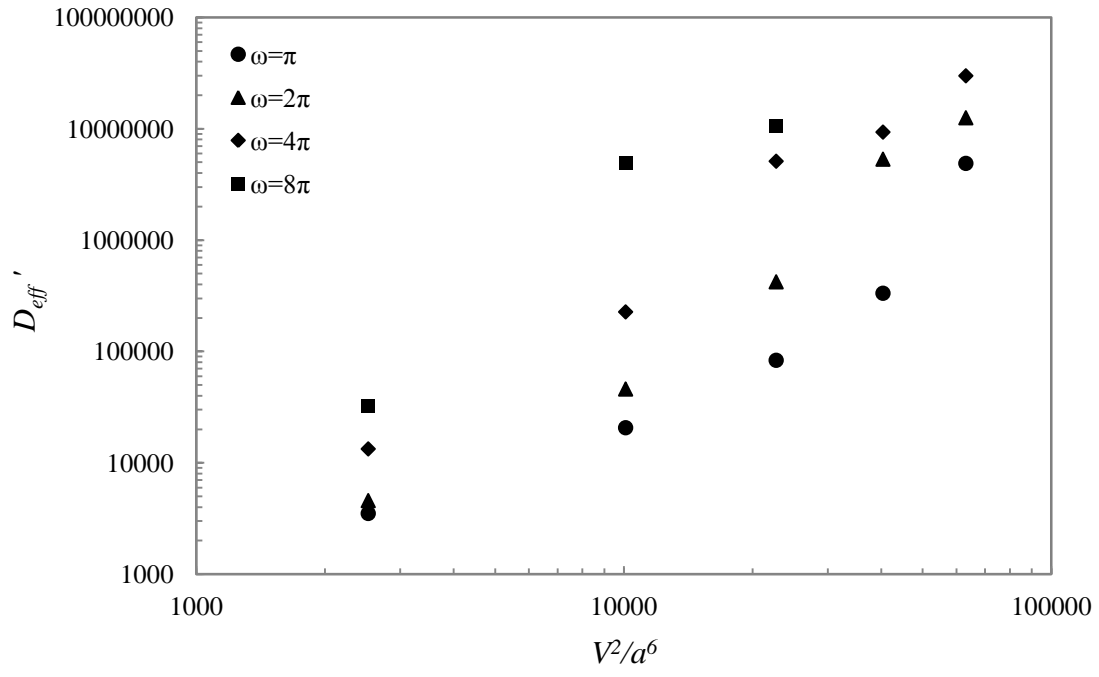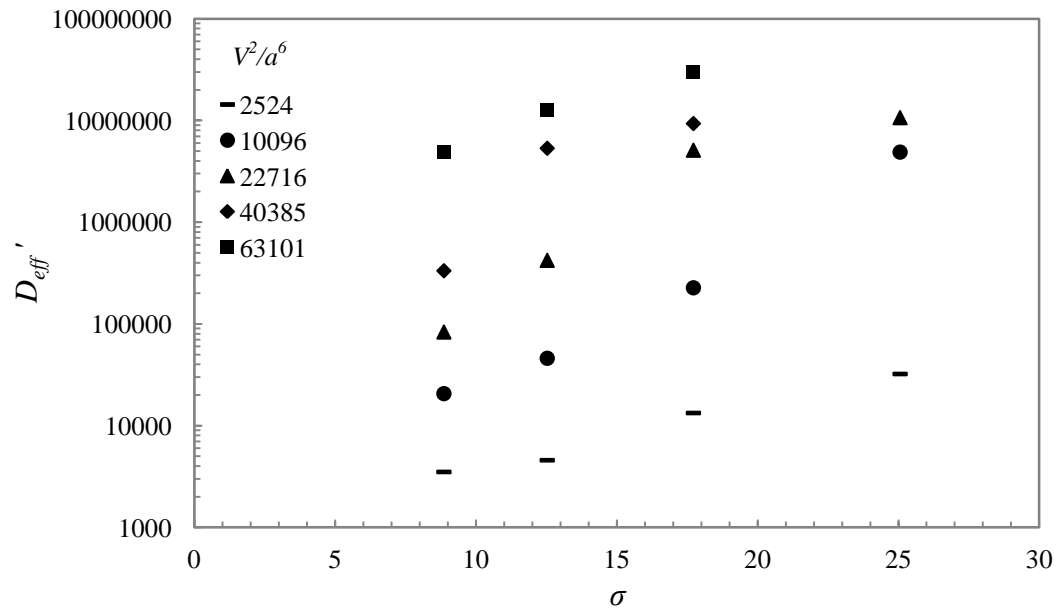($V = 18.8 \, \text{cm}^3$, $\omega = 2\pi \, \text{rad/s}$)

FIGURE 12. Concentration distribution as a function of distance from a maintained source

based on complementary error function

(a)

(b)

FIGURE 13. Variation of measured non-dimensional longitudinal dispersion coefficient with

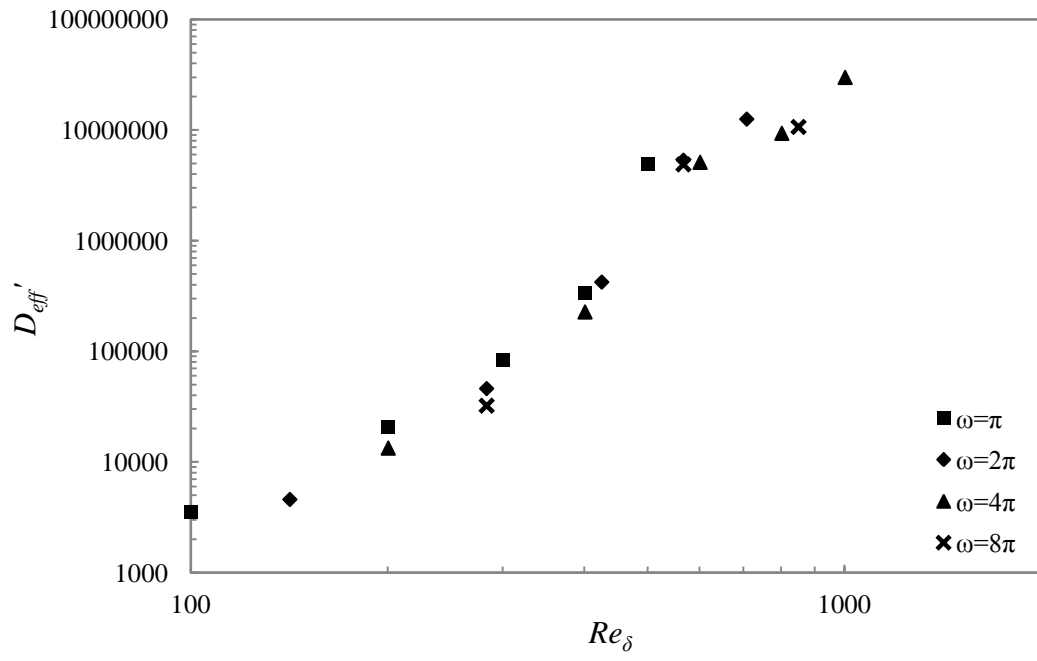(a) non-dimensional stroke volume and (b) Womersley number

FIGURE 14. Relationship between measured non-dimensional longitudinal dispersion
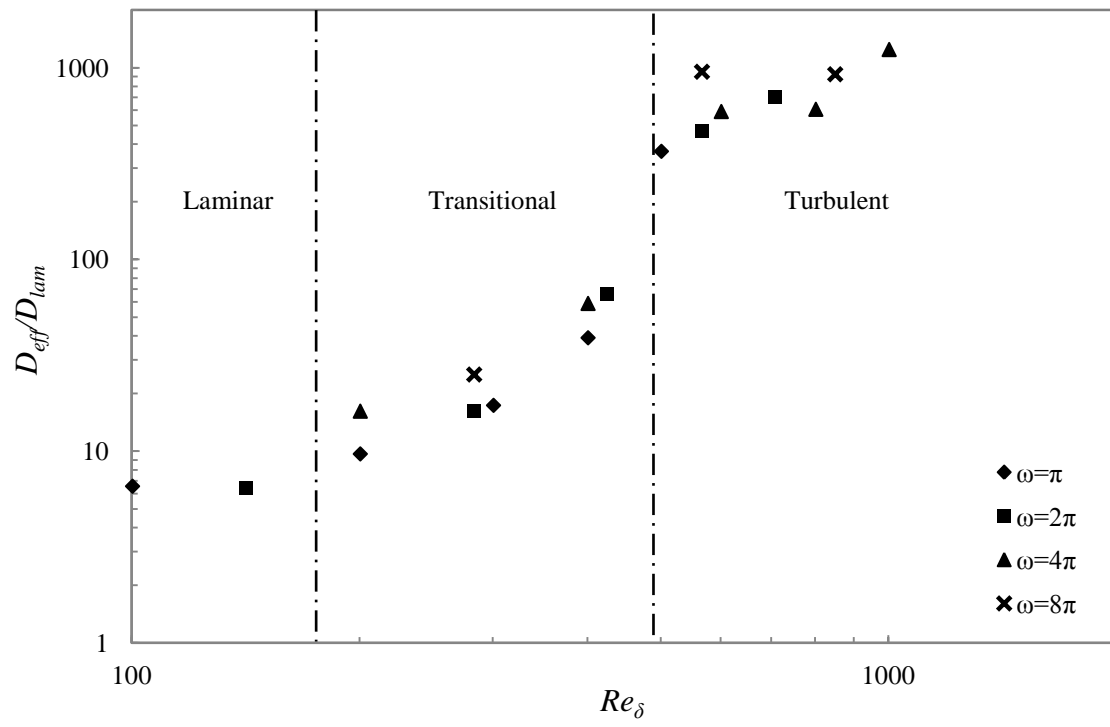
coefficient and Reynolds number

FIGURE 15. Comparison between experimental results and theoretical predictions for

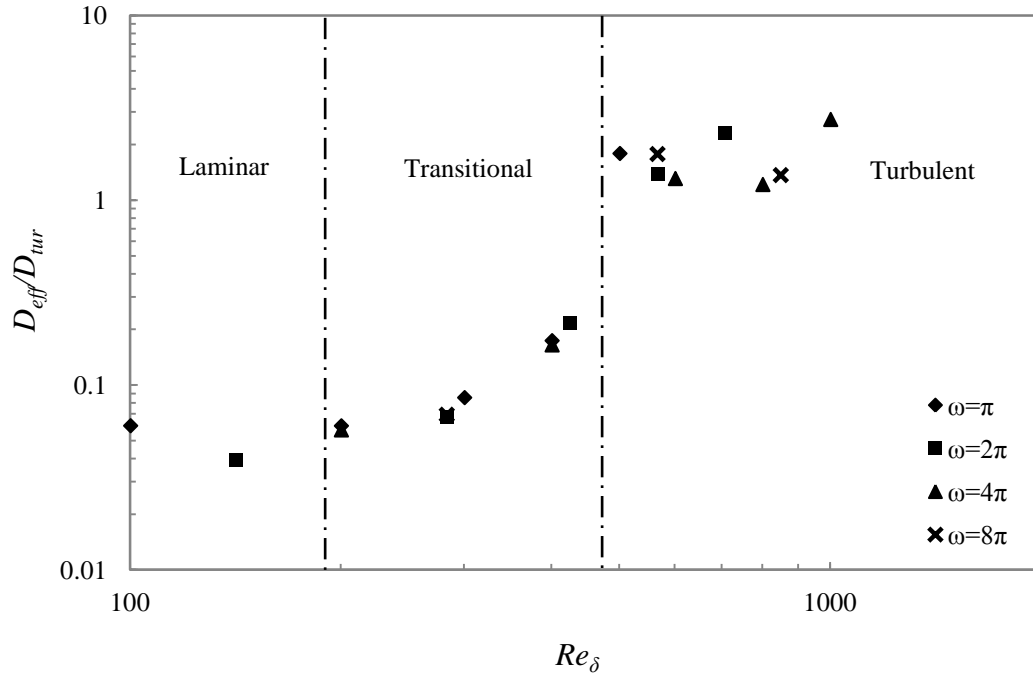laminar flows based on equation (54)

FIGURE 16. Comparison between experimental results and theoretical predictions for

turbulent flows based on equation (46)

Run	V (cm^3)	ω (rad/s)	U (m/s)	$\delta = \sqrt{2\nu/\omega}$ (m)	$\mathrm{Re}_\delta = U\delta/\nu$
1	6.3	3.14	0.126	0.000798	100
2	6.3	6.28	0.251	0.000564	142
3	6.3	12.56	0.502	0.000399	200
4	12.6	3.14	0.251	0.000798	200
5	6.3	25.12	1.005	0.000282	283
6	12.6	6.28	0.502	0.000564	283
7	18.8	3.14	0.377	0.000798	301
8	12.6	12.56	1.005	0.000399	401
9	25.1	3.14	0.502	0.000798	401
10	18.8	6.28	0.754	0.000564	425
11	31.4	3.14	0.628	0.000798	501
12	12.6	25.12	2.009	0.000282	567
13	25.1	6.28	1.005	0.000564	567
14	18.8	12.56	1.507	0.000399	601
15	31.4	6.28	1.256	0.000564	709
16	25.1	12.56	2.009	0.000399	802
17	18.8	25.12	3.014	0.000282	850
18	31.4	12.56	2.512	0.000399	1002

TABLE 1. Summary of the experimental conditions